Pump Health Monitoring Test Environment for Diagnosing the Erosive Effects from Cavitation

Tedja Verhulst[1], David Judt[1], Craig Lawson[1], Osama Al-Tayawe[2], Geoff Ward[2] and Yongmann Chung[3],

[1]*Cranfield University, Cranfield, Bedfordshire, MK43 0AL, United Kingdom*
tedja.verhulst@cranfield.ac.uk
david.judt@cranfield.ac.uk
c.p.lawson@cranfield.ac.uk

[2]*Airbus Operations UK, Bristol, Gloucestershire, BS34 7PA, United Kingdom*
osama.altayawe@airbus.com
geoff.ward@airbus.com

[3]*University of Warwick, Coventry, Warwickshire, CV4 7AL, United Kingdom*
Y.M.Chung@warwick.ac.uk

Abstract

Cavitation occurs frequently in pumps. The subsequent erosion that is caused by cavitation can significantly reduce the operational efficiency and Remaining Useful Life (RUL) of the pump. This study describes a new hybrid Health Monitoring (HM) test environment, used to diagnose permanent damage caused by cavitation erosion in a two-stage centrifugal pump. Flowrate, pressure and motor current measurements are made and compared to Computational Fluid Dynamic (CFD) results. The hybrid-based HM carried out using the three methods provide the facility to develop diagnostics for cavitation erosion damage. The suggested methods will not only aid in HM development, but also select the best operating conditions to carry it out. The Gray Level Method (GLM) is implemented using CFD to predict the erosion areas in the centrifugal pump. A Simscape model is devised to enable development of health monitoring algorithms. Few works have attempted to detect for erosion caused by cavitation. It was found that a high-level agreement was achieved between the Simscape, CFD and test-rig results, with an average error of 0.8%, 2.5%, and 2.0% for current, pressure and flow measurements respectively. The results from this research show the feasibility of developing HM algorithms to detect cavitation erosion in aircraft fuel pumps by fusing model and data-based methods. This is an enabler for a move from time-based to condition-based maintenance, thus reducing aircraft operating costs.

https://doi.org/10.36001/IJPHM.v16i1.4207

1. Introduction

Cavitation is a problem for pumps as it causes significant wear. This phenomenon occurs when the liquid pressure falls below vapor pressure, promoting the growth of bubbles. These bubbles then implode and erode the impeller surface, causing permanent damage. This subsequent erosion damage reduces the operational efficiency of the pump and reduces its remaining useful life (RUL). The pump then cannot provide the required head and flows as the impeller geometry erodes over time. It is therefore highly beneficial to have the capability to diagnose for cavitation erosion and have a means of detecting its symptoms early.

Health Monitoring (HM) is defined as the field of diagnosing faults or predicting the Remaining Useful Life (RUL) of the pump. HM implementations can either be model (Maulana, Starr, & Ompusunggu, 2023) or data-based (Dessena, Ignatyev, Whidborne, Pontillo, & Fragonara, 2022) or a combination of both (Niculita, Jennions, & Irving, 2013; Skaf, 2015), where the latter is called hybrid-based HM. A more detailed description of HM and differences between approaches can be found in the works by Skaf (2015). According to Kahlert (2017), developing an HM test-environment to diagnose for cavitation erosion is highly beneficial, as it allows operators to monitor the pump condition and prevent unexpected breakdowns that can lead to financial loss. This maximizes the utility of the pump, reduces downtime and provides financial savings. The present maintenance strategy for many pump operators relies on time-based methods, where the pump is inspected or replaced after a certain number of operation hours or upon failure. The former type of maintenance is called preventative maintenance, while latter is called breakdown maintenance. An extensive review for common faults and the state-of-the art of airborne fuel pumps HM can be found in the works by Verhulst, Judt, Lawson, Chung, Al-Tayawe & Ward (2022).

Performing diagnostics to detect erosion, creates the capability for fault detection and fault prediction. A difficulty in monitoring incipient cavitation to conduct HM, is that the severity of the problem is only weakly influenced by the present health of the pump and more strongly by its surrounding environment and operating conditions. Monitoring erosion effects instead, gives the ability to observe changes in behaviour over time, as the permanent change to the impeller geometry is tracked. Incipient cavitation on the other hand, is a transient event over a brief time interval. The amount of material thickness loss (in mm) of the impeller can be correlated to its health; the severity of which can be detected by monitoring motor current, flowrate, and pressure. The changes in those parameters can be linked with a suitable HM technique, to quantify the magnitude of erosion and estimate the pump's RUL.

Past works have been carried out to perform HM on water pumps for cavitation erosion from Adamkowski, Henke & Lewandowski (2016) using vibration sensing only. Wang, Zuo & Fan (2011) describes a test-rig used to carry-out HM to detect for wear caused by slurry erosion, but only discusses the setup without the results. Another data-based method for aircraft fuel pumps by Jiao, Huang, Li & Xu (2017) uses vibration monitoring to distinguish different pump faults but does not propose a scheme to detect for an eroded impeller. Previous works by the various authors (Addie & Sellgren, 1998; Bross & Addie, 2002; Rayan & Shawky, 1989; Xu, Chen, & Xu, 2019) describe the damage and performance penalties caused by slurry erosion but does not suggest an HM scheme to detect it. Slurry erosion is like cavitation erosion, but the wear is caused by fine particles in the fluid.

Previous CFD simulations on cavitation erosion have been focused on the visual study of the vapor fractions and identifying erosion areas. Previous works such as by Dular, Bachert, Stoffel & Sirok (2004), Dular Stoffel & Sirok (2006), Dular & Coutier-Degosha (2009), Usta et al. (2017) as well as Li & Van Terswiga (2012) have respectively developed the field functions to predict erosion and tested it on single-stage pumps, propellers and aerofoils. The works by Dular et al. (2006) used an erosion model initially developed by Fortes-Patella, Reboud & Briancon-Marjollet (2004) through experiments carried-out on an aerofoil. The work carried out by Verhulst, Ng, Chung, Judt, & Lawson (2022) extends the previous works by predicting erosion damage on two-stage pumps.

This paper describes a hybrid-based HM scheme to detect for cavitation erosion, where a combination of data and model-based HM is conducted to diagnose the current health state of the pump. The first part gives a brief literature review related to current state of Health Monitoring (HM) technologies related to cavitation erosion. The second part provides an overview of the entire test-environment and experimental plan; outlining how the test-rig, CFD and Simscape models are used to conduct hybrid-based HM. Finally, a comparison is provided in the results section with a non-eroded impeller to highlight the data alignment between the three methods.

The focus of this portfolio submission is to give an overview of the experimental test-rig as well as to understand its capabilities and limitations by comparing experimental and baseline model data. The proposed fault testing scheme uses the erosion wear areas as identified by Verhulst, Ng, Chung, Judt, & Lawson (2022) and artificially creates erosions on the impeller as a means of accelerated fault testing. This work therefore extends the findings from the Gray Level Method (GLM) Dular et al. (2006) to project the wear areas, experimentally test artificially eroded impellers, and to then develop an HM scheme. The test-rig system flow and pump head rise data are gathered to determine the appropriate operating points for the pump and later linked to the HM method. Current sensors are used in each of the three phases of the motor terminals to conduct an Electrical Signature Analysis (ESA). These types of sensors are chosen, as they are largely non-intrusive and low-cost when compared to torque, acoustic and vibration techniques (Benbouzid, et al., 2021). This is highly desirable for simple but also cost-effective implementations of HM.

2. LITERATURE REVIEW

2.1. Cavitation Theory

Cavitation occurs when the liquid pressure is below the vapor pressure. According to Messina, Cooper & Heald (2008) for centrifugal pumps, the impeller eye is often considered to be the most vulnerable region, as this is the point at which the static pressure is the lowest in the entire pump. The damage mechanism caused by cavitation creates a sandpaper-like surface on the impeller. Erosion has been known compromise operational efficiency, as highlighted in the works by the various authors to evaluate for erosion damage to pumps in (Addie & Sellgren, 1998; Bross & Addie, 2002; Rayan & Shawky, 1989). This is caused by the pump needing to rotate faster to achieve the same desired head and flow. Walker (2001) and Walker & Roudnev (2002) found that the differences are that slurry erosion is caused by fine particles and the wear is spread evenly across the pump. The erosion can become so severe, that the pump can no longer function at its intended operating point. These works discuss the damage mechanism and performance penalties caused by erosion, but no HM technique is proposed. Vapor fraction is the most common parameter used to observe for cavitation in most simulation techniques, as it gives some indication where the bubbles are concentrated but does not accurately portray the erosion-sensitive areas. It quantifies the ratio of vapor to liquid that is present, and is expressed between a value of 0 and 1. Further reading on cavitation and examples of how vapor fraction is utilized to express the severity cavitation is available in the works carried out by the various authors (Sedlar, Zima, Bajorek, & Kratky, 2012; Visser, Dijers, & op de Woerd, 2000; D'Agostino, 2011; Zhu & Zhang, 2017).

2.2. Previous Works for Cavitation Erosion

The Gray Level Method (GLM) was devised by Dular et al. (2006) and experimentally validated against the work by Bachert, Ludwig, Stoffel, Sirok & Novak (2003). This method been chosen to predict for erosion on the pump used in the test-rig discussed in Section 3. The GLM method mathematically estimates the gray intensity values and portrays them as an image, which can be used to distinguish the erosion-sensitive areas on the metal surface. These intensity values depict areas which are more at risk to erosion.

GLM has demonstrated its accuracy in predicting erosion on a centrifugal pump and hydrofoil. Unlike all the other techniques discussed, it can both identify and quantify the erosion-sensitive areas. The implementation of GLM involves the calculation of jet velocities and associated deformation on the pump surface, which is detailed further in Section 3.3 More details of the process of how the erosion areas predicted by CFD can be found in the works by Verhulst, Ng, Chung, Judt, & Lawson, (2022).

A 1 kW Brushless Direct-Current (BLDC) motor is used to power the pump. BLDC motors move by using the magnetic field generated by the stator coils. The attraction caused by the opposing polarity stator and rotor poles generates torque and creates rotational motion. More in-depth description of BLDC motors can be found on the work by Hughes and Drury (2019).

Alternating Current (AC) motors are not suitable for the purposes of HM. The stator currents and voltages measured on AC motors are not as sensitive to changes to speed and torque, unlike its BLDC counterpart. This sensitivity allows the motor stator currents to react to flow and pressure changes caused by the eroded impeller, which allows electrical signature analysis (ESA) to be carried out. ESA refers to an HM technique that relies on the changes in the current signal because of the fault. More information on the fundamentals of ESA can be found on the work by Rajagopalan, Aller, Restrepo, Habetler, & Harley (2006).

2.3. Electrical Signature Analysis

Motor current and terminal voltage monitoring fall under the category of electrical signature analyses (ESA), the pumps faults are monitored of the motor electrical parameters (Benbouzid, et al., 2021). ESA relies on placing current sensors across each motor phase that is connected to the pump. For a BLDC motor, the benefits of vibration monitoring are superseded by ESA as many of the changes that can be detected by vibration can also be detected using motor currents. Previous works has shown that the frequency and amplitude of mechanical vibrations and are related to the magnitude of the stator currents measured at the motor phases. More information on the basics of ESA for electric motors can be found in the work by Rajagopalan et al. (2006) ESA has the added benefit that the sensors have much longer life, as they can be installed at a distance away from the mechanical component and do not get exposed to the vibration which reduces the life of the sensors themselves. Furthermore, Current Transformers (CT) do not make physical contact with the mechanical and electrical parts of the pump, and are therefore not intrusive.

2.4. Erosion Test-Rigs

Few past works have conducted hybrid-based HM to diagnose cavitation erosion. One similar example is a test-rig devised for a UAV fuel system by Niculita et al. (2013), but designed to detect general fuel system faults, such as clogged valves and leakage flows.

Sarma, Tuohy & Djurovic (2019) have devised a test-rig tailored to detect stator and rotor-related faults for a generator unit used on a wind turbine. The test-rig attempts to re-create the setup used by a wind turbine but in a lab environment. Similar to the hybrid-HM setup described in this paper, The setup also utilizes a system model running on MATLAB in addition to the experimental rig, so that hybrid-based HM can be carried out. The subsequent work by the same research group Sarma, Tuohy & Djurovic (2021) and Sarma, Tuohy, Mohammed, & Djurovic, (2021) builds on the validated test-environment and describes the results for their HM scheme.

Adamkowski et al. (2016) carried out HM diagnosis of cavitation erosion using a purely data-based approach through vibration sensors. This method was successful in that it was able to use the resonance in the vibration signal to detect the severity of erosion. Another data-based HM exercise for aircraft fuel pumps by Jiao et al. (2017) also used vibration monitoring and showed successful identification of four types of faults through a single axis vibration sensor signal. The investigated faults, however, were not erosion related.

Wang et al. (2011) described a test-rig setup to detect wear caused by slurry erosion using data-based HM with vibration sensors. The authors of the mentioned work conducted accelerated fault testing by artificially re-creating the erosion wear. The damage profiles are approximated using statistical data gathered from the field. No mention has been made on the success of the HM techniques, but the methods have been used across different industries to diagnose the same problem. The work does not outline the success of the devised test set-up, but the methods and materials suggested in this work are based on field experiences.

Slurry erosion has been known to significantly reduce the pump operational performance, as highlighted by the various authors to evaluate for erosion damage to pumps in (Addie &

Sellgren, 1998; Bross & Addie, 2002; Rayan & Shawky, 1989; Xu, Chen, & Xu, 2019; Ylonen, 2016). This is caused by the pump motor needing to produce more power to supply the same head and flow. The differences are that slurry erosion is caused by fine particles and the wear is spread evenly across the pump, whereas cavitation erosion is caused by imploding bubbles that deform the surface.

The general method outlined in Section 3 focuses a hybrid-based HM, where model and data-based approaches are combined, with advantage of having the possibility for more advanced detection and prediction algorithms as part of future work. In addition, for future expandability of HM techniques, the multiple sensing methods used by the test-rig discussed in this paper allows a comparative study to be carried out. The results from this can provide advice on which HM is most practical and reliable to diagnose for cavitation erosion. The test environment is designed specifically to detect cavitation erosion damage on centrifugal pumps. It also operates at significantly higher pressures and flowrates than the previous referenced work.

3. MATERIALS & METHODOLOGY

3.1. Test-Rig Configuration

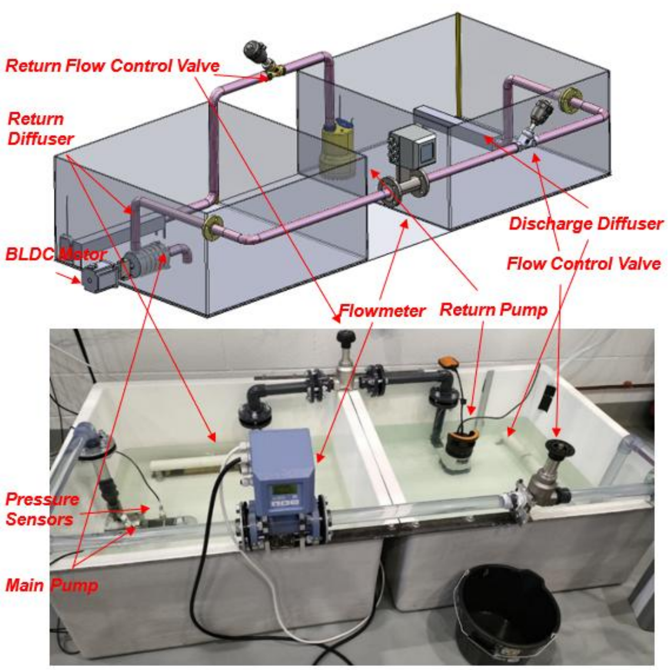

Figure 1. Test-Rig 3D-render and actual installation on-site.

The primary goal of the HM test-environment is not to stimulate pump cavitation and detect it, but to detect the damage caused by the subsequent erosion and have a diagnostic technique that can differentiate various levels of its severity. The test-rig 3D-render is portrayed in Figure 1 (top) and actual installation (bottom)

3.1.1. Main Pump

The main pump being used in the experiment and modelling activities is a centrifugal pump with a two-stage impeller. It has a 1.25-inch inlet (31.75 mm) and a 1.0-inch (25 mm) outlet, the diameter of the impeller is 95mm and the pump case is 100 mm. The impeller has blade has 5 blades, but its specific speed and blade curvature are not specified by the manufacturer. The head-flow performance curve of the pump is outlined in Figure 15a, while blade geometry is depicted in Figure 14. In addition to being representative of many pumps in industry, this specific pump model is chosen as spares are widely available in the market, making it practical and cost-effective for carrying out fault-related experiments.

3.1.2. Tank Design and Piping Installation

The test-rig uses a two-tank layout so that the outgoing fluid flow does not create disturbance in the main tank. The tanks have a capacity of 400L. The pump is submerged in water and mounted on the side of the tank as this is the most practical installation of a submersible pump. A snorkel is installed in the inlet to decrease the unusable fluid level. The tank is created out of Glass Reinforced Plastic (GRP) for strength. The pump centre of rotation is placed 110mm above the base of the GRP tank to allow ease of installation with the motor components outside the tank. Figure 2 depicts the process diagram of the test-rig setup.

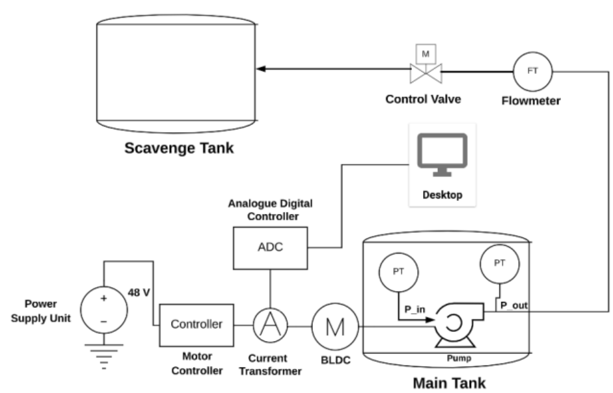

Figure 2. Schematic view of Test-Rig.

The pipe material chosen is transparent PVC, as it meets the operating pressures of the pump and allows the flow to be visually monitored for any abnormalities. A pipe with 1.25-Inch (31.75 mm) inner diameter is chosen so that the entire cross section is filled with water under normal operating conditions. This pipe diameter allows a fluid velocity of over 0.5 m/s under the lowest operating flowrate, and near 3 m/s on the highest, which ensures reliable operation of the magnetic flowmeter. The total pipe length is approximately 5m so that other test-rig components such as pipe elbows, flowmeters and valve can have the required pipe distance between each other.

3.1.3. Motor Details and Installation

A 1 kW, 48VDC BLDC motor is used to power the pump The model of the motor is the D110BLD1000-48A-30S and controller is BLD-50A both by DMKE. The supply voltage is connected to the motor controller unit. The controller receives the motor hall-effect sensors as inputs, and then outputs the voltages to the electric motor. The motor has an operating speed of 0 to 3500 RPM, which can be modulated via a potentiometer, voltage or frequency input in the controller interface.

3.1.4. Pump Control Strategy

The pump speed is operated at either 2900 RPM, or 3500 RPM as recommended by the pump manufacturer. Operating the pump above or below these speeds is not recommended, as it is outside the intended operating points by the manufacturer. The impeller may be operated outside the pump rotors' specific speed, and thus the head-flow characteristics may deviate from the known characteristic behaviour. Operating between these mentioned speed boundaries is also possible, but there will be no reference data from the manufacturer datasheet to validate the data with. To modulate the flow a globe valve is used. Throttling the valve moves the operation point of the pump along the head and flow, while varying the motor speed shifts head flow curve diagonally as highlighted in Figure 15a. The BLDC motor has its own controller unit that controls the switching electronics for motor speed regulation using Pulse-Width Modulation (PWM) at a switching frequency of 10 kHz. This controller is a Proportional Integral and Derivative (PID) cascade controller with a speed outer loop and a current inner loop. The values of the gains and stability limits are not specified by the manufacturer. The model running on Simscape was manually calibrated until the performance of the two systems matched.

3.1.5. Data Acquisition Unit

The motor is operated at a maximum of 3500 RPM, which is equivalent to rotation frequency of 116.67 Hz. The fundamental frequency when performing frequency-domain analysis for the current signature is widely accepted to be up to the 10^{th} harmonic (1166.7 Hz), above which one will experience significant attenuation with resulting small signal noise ratios (Wang, Zuo, & Fan, 2011). According to Nyquist Sampling Theorem, the minimum sampling frequency should be at least twice the signal of interest, but a sampling frequency of ten times the signal of interest is recommended for improved signal resolution (Kehtarnavaz, 2008). Following the latter recommendation, yields a minimum sampling frequency of 11.67 kHz. The Texas Instruments ADS8588SEVM-PDK is used as the data acquisition unit for its high sample rate in each channel. This unit has a dedicated Analogue Digital Controller (ADC) on each of its 8 inputs with a sample rate of up to 200 kHz on each channel, allowing simultaneous data capture of multiple sensors. A sampling rate of 50 kHz is chosen as this is twice the sensing bandwidth of both the pressure and current sensors at 25 and 23 kHz respectively, and to keep data sizes manageable. The ADC can accept input voltage ranges of ±10V on its analogue inputs with a resolution of 16 bits, so it is compatible with most of the selected sensors.

3.1.6. Sensor Specification and Installation

Current, flow, pressure and temperature sensors are installed on the test rig. The installation points of the sensors on the test rig are defined as follows:

Current Sensor: WCS1800 CTs are placed between the motor input terminals and the output of the inverter bridge circuit, so that each of the three motor phase currents can be individually measured. This component is connected Integrated Circuit (IC) on a board which amplifies the CT output signal before reaching the ADC. CTs are used for current sensing as it does not make a direct electrical connection with the motor, protecting the ADC from large currents and voltages that the unit is not rated for. CTs measure the current value by measuring the change in magnetic field because of the BLDC trapezoidal current profile in each of its three phases. This model sensors can measure the current up to ±35A and has a bandwidth of 23 kHz. The current output does not exceed 25A peak for each phase. The extra 10A headroom allows sufficient headroom to capture large spurious transients that may appear during the fault-testing phase. The CTs convert the measured current at a rate of 0.08A/V, meaning that the sensors will output 1V to the ADC, for every 0.08A measured. At 0A, the current sensors output a voltage of 3.7V. This is intended, as this drift voltage from the built-in ICs is used to indicate that the sensor is functioning as intended. The sensors outputs 1V at 0A when it is faulty.

Day #	Pressure (m)	Flowrate (l/s)	Current (A)	Temperature (^oC)
1	0.53	0.00	0	1
2	-0.93	0.01	0	-1
3	0.10	0.01	-0.125	1
4	-0.82	-0.01	-0.125	0
5	0.21	0.02	0.15	1

Table 1. Offset values from sensor readings over 5 days

Flow Sensor: The Burkert SE56 magnetic flowmeter as this technology provide the greatest resilience to pipe vibrations and shockwave disturbances from the pump. The distance between the neighbouring pipe bend and the valve is placed 5 pipe diameters (159mm) as this is the distance recommended by the manufacturer to eliminate any flow disturbances caused by the adjacent components. The output of the flowmeter is set as an impulse and frequency on both of its channels to represent the same flowrate output in different ways. The impulse output signal is a duty cycle between 0 to 100% between the maximum and minimum flowrate of the system specified by the user, which in this case is 0.25 l/s and 2.5 l/s. The frequency output generates a maximum frequency of 100 Hz at the maximum flowrate and 10 Hz at the minimum. Any flow abnormalities such as reverse flows can be detected by visual inspection of the transparent pipe or by alarm outputs of the sensor. For magnetic flowmeters, the pulse and frequency outputs are preferred over 4-20mA signal for HM application, as it is representing the captured signals in its most raw form, ensuring that no information is lost.

Pressure Sensors: Two Burkert 8316 pressure transmitters are installed on the test rig pipes placed two pipe diameters away (63.5mm) on the respective pump inlet and outlets. This model is chosen as it is within the measurement range to capture the pump head rise of 0-40m and has a bandwidth of 25 kHz. The sensor outputs a 4-20mA signal and is interfaced a termination resistor of 250-ohm that converts the output range to 1-5V to represent the pressure range to the ADC. The method of installation and parameter extraction follows the standard outlined by ISO 9906 Annex A (International Organisation for Standardisation, 2012). The sensors are installed at two measurement points, so the pump head rise is accurately measured.

Temperature Sensor: A thermal imaging camera is used to monitor the temperature of the motor and record increases because of the erosion. This tool is advantageous as multiple areas of the system can be simultaneously monitored. The camera has a resolution of 1°C and saves the output as an image.

3.1.7. Sensor Calibration

Current Sensor: The CTs are calibrated by using a test circuit before being implemented into the motor in the test-rig. The circuit consists of:

- Simple bench power supply rated capable of outputting 15V, 10A.
- PWM generator rated of outputting 10 kHz signals.
- 3x 1-ohm chassis resistors, each rated to 5W.

The three elements of the circuit above are connected in series. The wire from the test circuit is looped inside the CTs for current measurement, which has its voltage output connected to an oscilloscope. Since the maximum current going through the wire is 5A with this circuit, the wires are looped 5 times to the CTs so that output replicates to similar ball-park values to the test-rig motor value of 25A peak. The current observed is multiplied by the number of loops going into the sensors.

Flow Sensor: Before a test-run, the flowmeter is calibrated to zero first with the pipe cross section full of water but movement of the fluid. The flow control valve is then set different open %. The time required to drain the tank by 100L informs the true average flow rate, which is done by a smartphone stopwatch. The timed flowrate is then compared with the flowrate displayed by the flowmeter recorded every 5 seconds and its average value used for comparison with the timed value. This method is useful to quantify the mean steady-state flowrate error and its general accuracy, but does not quantify the error caused by flow fluctuations. The tests were done at intervals of 0.5 l/s to simplify stopwatch timing and to cover the general span of the pump operating points. It was found that the main source of deviations is from the turbulence found at higher flow rates (>2.0 l/s). To prevent vortexing, the lowest point of the tank for this test is defined to be 10cm above, the snorkel and the highest is 20cm. The time it takes to drop the water by 10cm is used as the reference point as the true flowrate.

Pressure Sensors: Pressure sensors are calibrated by first turning on the sensors and checking the sensor output when no fluid is present and when submerged with water but with no pump flow. At this point the output of the pressure sensors is checked to ensure that it outputs 4mA as required, which corresponds to 1V when connected to a 250-ohm resistor. Once the flowmeter is calibrated, the pressure sensor can easily be validated. The same sweep of tests with different flowrates are carried out, but this time the pressure sensor outputs are checked. The sensor outputs are compared with the values of the performance envelope from the pump manual at a specific flowrate. This is to check for the level of agreement that the set-up has with the manufacturer data.

Temperature Sensor: To calibrate and investigate the accuracy of the thermal imaging camera, ice and boiling water tests were conducted. The temperature displayed by the crosshairs of the center image are recorded. The data was collected in intervals of 5 seconds for over 1 minute and the same test is repeated in a different day. The goal is to observe how accurate and to quantify the level of deviations from the measurement when it measures a different temperature.

3.1.8. Uncertainty Analysis

Every measurement is subjected is error and this issue is presented as follows by Eq. (1):

$$Measured\ Values = True\ Value\ \pm Error \tag{1}$$

The error bars which are calculated from Eq. (2) are based on the work by Chowdhury, Ali & Jennions (2023).

$$Error = \sqrt{(Accuracy\ Error)^2 + \ (Precision\ Error)^2} \tag{2}$$

The total error from each error is sourced from accuracy and precision errors. Accuracy outlines how the measured value disagrees with the true value, whereas precision error refers to the spread of the sampled data (Taylor, 1998). Chowdry et al. (2023) outlines that precision errors are caused by unpredictable changes in the experimental setup or surrounding environment and help quantify deviations from the mean values.

Figures 3 to 7 summarizes the error for a wide range of operating points used. In this section the sensor error is evaluated for two ambient temperatures 0ºC and 20ºC, to observe how the measurement taken at different days and ambient environmental temperatures could affect the results. The two temperatures are chosen as this is the range of temperatures in the test-rig location.

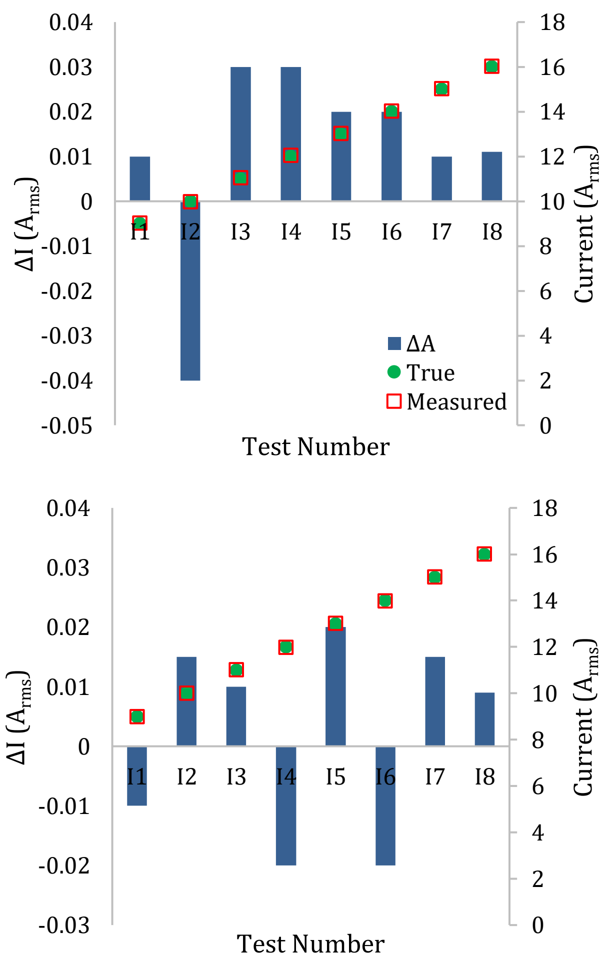

Figure 3. Scatter-plot comparing true and measured values of current sensors.

Offset Error: To quantify this error, measurements from all the sensors are in a 5-day period as summarized in Table 1. This is to gauge the effects of the environmental temperature and other possible sources of random error on the repeatability of the sensor readings. The sensor manufacturers did not provide a value related to the offset errors, so comment cannot be made about this parameter.

Current Sensor: A source error for this type of sensor is the discrepancy between the true value and current ripple from the PWM controller used by the BLDC. Figure 3 compares the results between the data captured from the bench supply compared with the output of the CT sensor, along with its discrepancy.

As highlighted by Figure 3, a maximum error of 0.029 A measured at approximately 25 A has been achieved from the discrepancy from the ammeter and the CT sensor. The bar chart indicates the value between the difference between measured and true values. this is insignificant compared to the errors generated by the PWM ripple currents, which are quantified to be 0.56A for the 3500 RPM case and 0.84A for 2900 RPM case, when measured from peak-to-peak of the ripples. This type of error is dependent on the rotating speed and has a fixed value for across all the pump operating points.

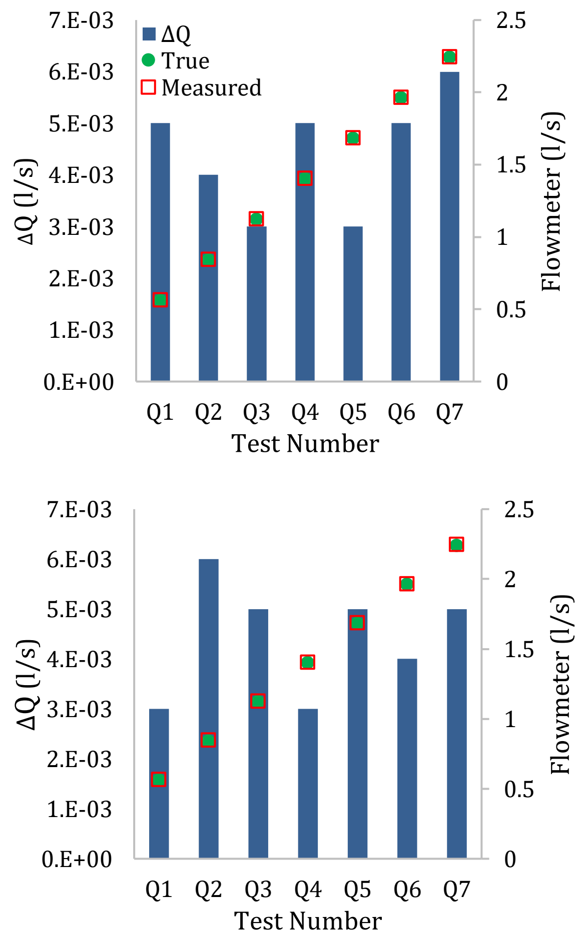

Figure 4. Scatter-plot comparing true and measured values of flowmeter data.

Flow Sensor: The errors from the flowmeter measurements are primarily from the limits of the measurement tolerances of the device and the flow fluctuations from turbulence (Hayward, 1979).

Figures 4 and 5 outline the flowmeter data comparing true and measured values. The bar chart on Figure 4 indicates the discrepancy between the two values, whereas the bar chart on Figure 5 outlines the amplitude of the flowrate oscillations. The manufacturer has quoted a measurement tolerance of 0.2%. Both offset error and measurement tolerances are insignificant compared to the errors from the pulsating flows caused by turbulence. As highlighted by Figure 4, a maximum error of 0.006 l/s measured at 2.24 l/s has been achieved from the discrepancy from the stopwatch results and the flowmeter readings. The maximum error based on the maximum turbulence fluctuation is 0.013 l/s as outlined by Figure 5.

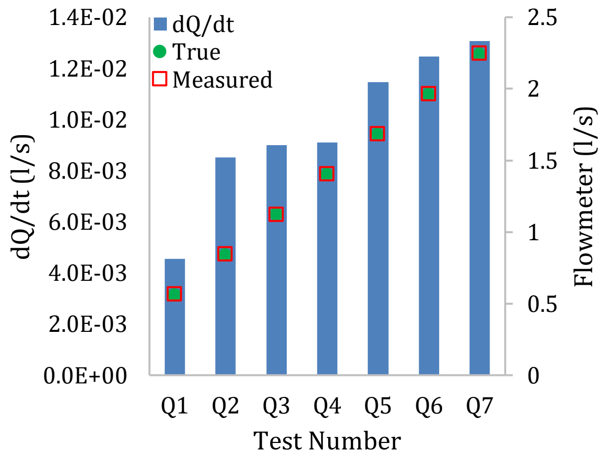

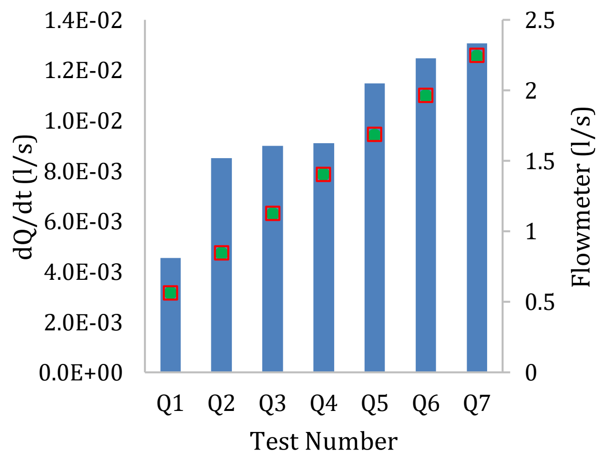

Figure 5. Scatter-plot highlighting flowmeter errors.

<u>Pressure Sensors</u>: These sensor readings are subject to different types of errors, such as: offset, hysteresis and non-linearity. The former two factors are influenced by the temperature of the fluid, but for liquid, especially water (H_2O) the effects are not as significant as measuring pressure with a gas such air (O_2). Investigating the precision of the pressure sensor, like the flowmeter required it being directly installed in the test-rig. The setup of the sensor, such as its position relative to the pump outlet and the method at which it was tapped into the pipe had an influence on its setup.

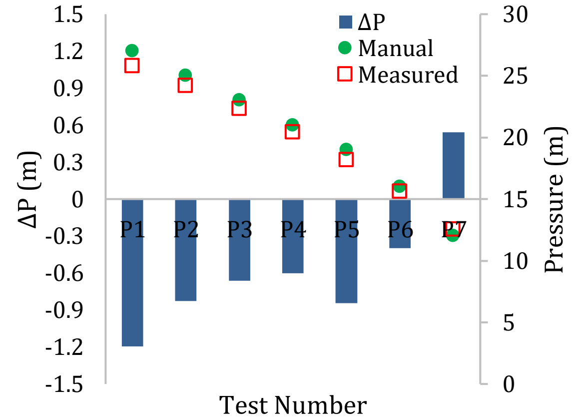

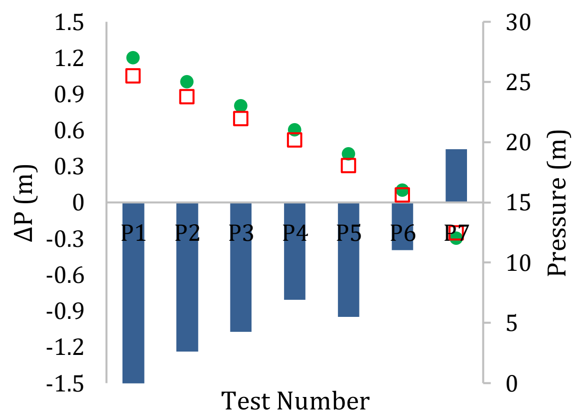

Figure 6. Scatter-plot comparing true and measured values of pressure data.

Figures 6 and 7 outline the pressure data comparing true and measured values. The bar chart in Figure 6 indicates the discrepancy between the two values, whereas the bar chart in Figure 7 outlines the amplitude of the flowrate oscillations.

The reference values are taken from the pump manual datasheet. A limitation of the comparison in Figure 6 is that the pump installation used to generate the manual data is slightly different to the pump setup used in the test-rig, leading to minor discrepancies between the two measured values. The setup in the test-rig is an open system with a snorkel to draw water from the tank, whereas the reference setup described in the manual is a closed system. The bar chart outlining the discrepancy in Figure 6 to provide some form of reference on the pressure readings and how it conforms with the manual, however these error values should not be relied upon for quantifying the errors for the reasons previously stated. The pressure error is primarily quantified by the amplitude of the pressure oscillations from the steady-state value outlined in Figure 7.

The pump head and flow curve from the manufacturer was used as a form reference point in-spite the slight difference in the setup. This is to give an understanding on the conformity the test-rig with the referenced value from the manual. Since a high level of accuracy has been achieved from the flowmeter tests, the flowmeter readings can be relied upon when choosing an operating point for the pump.

Temperature Sensor: An error of 1°C has been based on readings taken from multiple days. Any changes to the temperature readings are not caused from the motor reacting to the erosion damage, but due to changes in the ambient temperature.

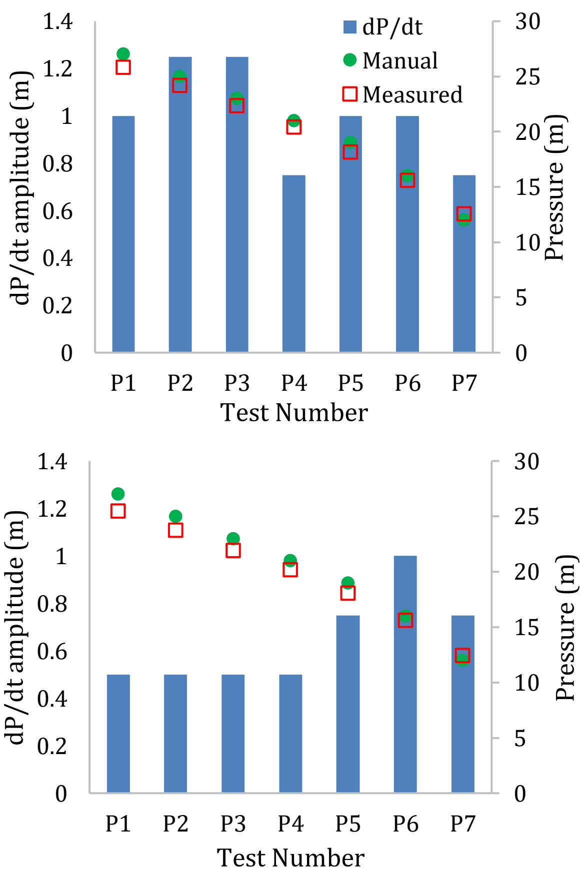

Figure 7. Scatter-plot highlighting pressure sensor fluctuations.

Eq. (3) summaries the accuracy of each sensing method for the pump operating at 0.56 l/s 3500 RPM, when all the error sources for each measurement value are calculated using Eq. (2) in the format of Eq. (1). Note that each operating point has different error values and that the errors listed in Eq. (3) serve as an example. The results summarise the error after six test runs for the same operating point. Further details on the sweep of tests from these six runs can be found in section 3.6.

$$\begin{gathered} \textit{Measured Pressure Values} = \textit{True Value} \pm 1.16\ m \\ \textit{Measured Flowmeter Values} = \textit{True Value} \pm 0.0091\ l/s \\ \textit{Measured Current Values} = \textit{True Value} \pm 0.40\ A \\ \textit{Measured Temperature Values} = \textit{True Value} \pm 1\ ^{o}\ C \end{gathered} \tag{3}$$

The tests carried out in this section are preliminary tests to outline the level accuracy across a wide range of operating points being measured by each sensor. It provides examples on how the uncertainties are calculated and is meant to give a sample calculation to the error values corresponding to a specific pump operating point for its pressure, flow, current and temperature measurements. It also outlines which of the multiple sources of measurement errors for each sensing method are the most significant contributor to the quoted uncertainty values. The data in this section also is meant to highlight the variability in the sensor readings when the data is captured at different days and ambient temperature conditions.

Normality of Data: The 6 samples taken for each data point in the test-rig has been run with the Shapiro-Wilk test (Shapiro & Wilk, 1965). This is the most reliable method to test for normality when the sample sizes are less than 50 (Mishra, et al., 2019; Hanusz & Tarasinska, 2011). Histogram, Q-Q plot and Skewness tests are also reliable test to check for normality, but only when the sample size is at least 50 (Mishra, et al., 2019). Based on the null hypothesis results from the Shapiro-wilk test, the collected datapoints conform to a normal distribution. Further reading on the Shapiro-Wilk test can be found on the work by Shapiro & Wilk (1965) and Hanusz & Tarasinska (2011)

3.2. Test-Rig Simulation Model

The simulation model of the test-rig running on Simscape, depicted by Figure 8, is used to produce additional model data for the purpose of the HM algorithm development. The model is implemented using the MATLAB/Simscape environment and makes use ‘thermal liquid’ (TL), mechanical and electrical domain components. This software package is used for the system model as it provided a sufficient level of fidelity to carry out model-based HM, as highlighted by previous works for diagnosing motor-related faults by Sarma, Tuohy & Djurovic (2019), Sarma, Tuohy & Djurovic (2021) and Sarma, Tuohy, Mohammed & Djurovic (2021). It also has the advantage of doing multi-domain physics simulation, so all the parameters of the test-rig can be simulated in a single model. This ensures fluid property variations due to temperature are accounted for.

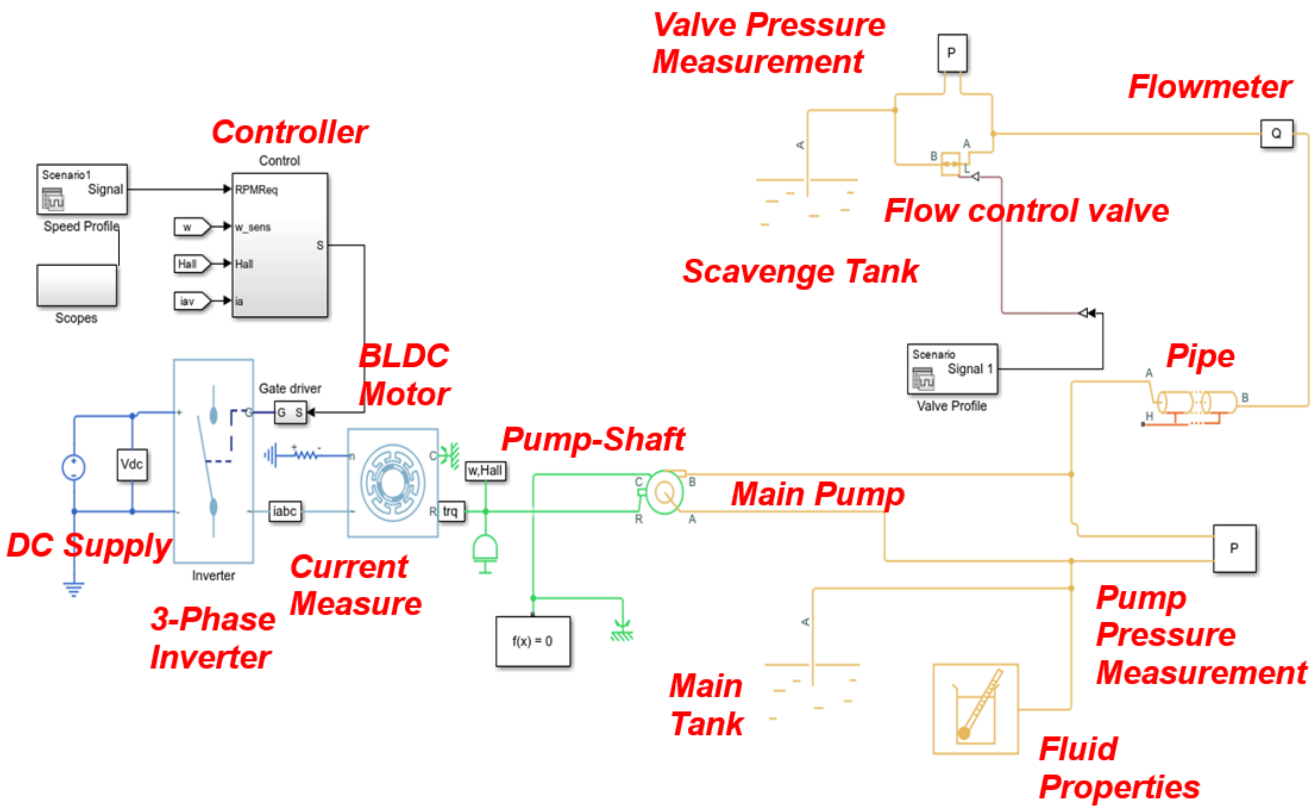

Figure 8. Simscape simulation set-up.

3.2.1. Electromechanical Components

BLDC Motor: The motor is modelled to reflect the component that is installed on the test-rig to power the pump. The phase currents are measured on each phase input of the inverter, in between the controller output. The motor has similar defining parameters as the installed unit. The BLDC model in Simscape models the electrical components as a resistor-inductor component. The user can define the pole number, the value of the resistor, inductor & and mutual inductances, as well as motor inertia. The stator winding architecture and back-EMF profile can also be defined by the user, but this has been defined as wye-wound and trapezoidal to represent the motor.

Pump-Shaft Interface: The pump shaft interface connects the BLDC motor block with the pump and defines the rotational inertia. A torque sensor is connected in the model but is not installed on the test-rig, mainly used to help tune the controller.

DC Power Supply: An ideal DC supply of 48V DC is used to represent the DC power supply powering the inverter.

Inverter: This element interfaces the 48V DC supply to the BLDC motor. The inverter converts the controller signals into voltages with the appropriate switching sequence to simultaneously power the motor and regulate its speed. The transistors are modelled as ideal components as at a low switching frequency of 10 kHz, the limitations of the transistors used are not apparent.

Current Sensor: An ideal current sensor is connected between 3-element wire outlined as 'iabc' to measure the current signals being output by the inverter going into the BLDC motor. The test-rig results have highlighted that the current ripples in the circuit are a greater source of uncertainty than the accuracy of the sensors themselves.

3.2.2. Fluid Components

Tanks: The two tanks are unsealed and are represented by the reservoir block with unlimited fluid quantity. The level of the fluid can be specified by the user to simulate the static head.

Pipe Segments: The pipe segment block used represents the pipe installation of the test-rig, such as the pipe length, diameter, material and surface roughness, and number of 90o pipe segments on the entire fluid path. The Reynolds number of the flow is also specified in this block and is chosen based on the CFD results.

Valve Block: The valve block is used to modulate the flow, and its coefficients are the same as on the valve used on the test-rig. It is modelled to open with an equal percentage, and the valve coefficients at different open % are defined in a look-up table. The parameters inputted to this component are based on the flow coefficients values outlined in the manufacturer datasheet for the valve.

Main Pump: is defined based on a look-up table with four elements: Pump rotational speed, and its corresponding input power, head and flow values at that speed. The parameters input to the model are based on the unit installed on the test-rig.

Return Pump: The return pump and pipes are not simulated as their task in the test-rig is only to refill the main tank and keep water level at the same value during the run of the simulation and is not measured for HM. The tank level and static head can be defined using the reservoir block that simulates the tanks.

Pressure Sensors: Two ideal pressure sensors highlighted by the ‘P’ block are used to monitor the head rise in the pump and subtracts the difference pressure measured at the inlet and outlet of the pump. The sensors are modelled as ideal because according to the test-rig results, the errors caused by the turbulence of the fluid is greater than the error caused by the accuracy of the device. The pressure sensor on the valve is not used on the test-rig but is kept in the model for troubleshooting purposes.

Flow Sensor: A single, ideal flowmeter highlighted by the ‘Q’ block is connected in series between the two tanks in the fluid path. Like the pressure sensor, the flow sensors are ideal as the errors is close to negligible, when compared to error caused by turbulence.

3.3. CFD Model

The areas mostly affected by cavitation erosion are identified using CFD simulations run with STAR-CCM+ as there are previous works that have accurately predicted cavitation using the same software package such as the work by Yilmaz, Atlar & Khorasanchi (2019) and Ge, Svenborg & Bensow (2021). The areas most affected by erosion effect are identified by implementing the GLM field function initially developed by Dular et al. (2006). STAR-CCM+ provides variations of the $k-\epsilon$ and $k-\omega$ to allow for the selection of different turbulence models depending on the application. The multiphase fluid model is used for H_2O provided by the fluid database in STAR-CCM+.

The $k-\omega$ shear stress transport turbulence (SST) model is used, as it combines the advantages of $k-\epsilon$, and the $k-\omega$ models. $k-\omega$ SST (Menter) applies the boundary layer estimation using $k-\omega$ formulation which allows the model to accurately estimate the boundary layers from the viscous sub-layer to the surface wall. Using an additional blending function, the $k-\epsilon$ behaviour is applied in the free-stream and avoids the common problem with $k-\omega$ in over-estimating boundary layer separation (Mao, Yuan, Pei, Zhang, & Wang, 2014).

Compared to other turbulence models, $k-\omega$ SST provided the relatively superior accuracy for estimating the boundary layers near and far from the wall surfaces for steady-state simulations (Yu & The, 2016). Its usefulness for unsteady simulations has also been validated Mao et al. (2014), Zhang (2017) and Deyou et al. (2015). A high level of alignment with experimental data was achieved in scenarios that have adverse pressure gradients and separating flows.

The eroded component is 3D scanned and re-assembled in software to replace the healthy component, the same as it would be in the test-rig installation. The pump in CFD is run at identical test conditions as the pump on test-rig, which is being submerged underwater. The performance of the impeller is tested, and the HM parameters of interest are monitored, except for motor currents, as this is not possible to be monitored in CFD. After ensuring that the data from the test-rig and CFD are consistent, the differences between the healthy and eroded impeller are analysed. This is to understand whether the erosion causes any noticeable change to the monitored parameters and an HM solution can be developed. The differences because of the erosion will create the adjustment factors in the model being run in Simscape.

3.3.1. Simulation Set-Up and Meshing

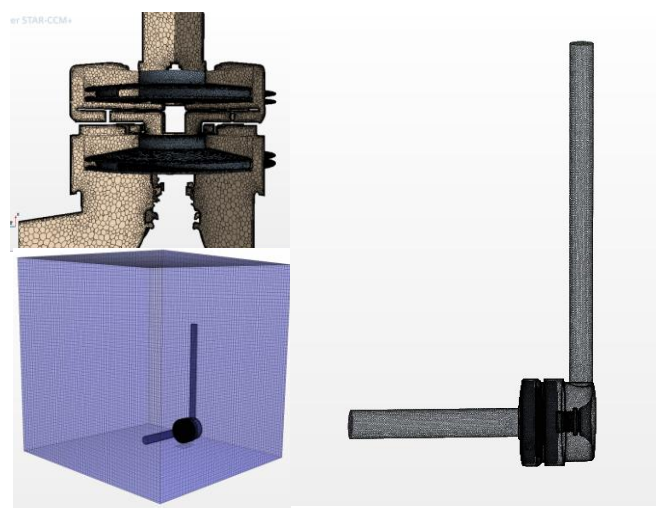

Figure 9. Pump CFD setup, clockwise from right: Pump and pipe geometry, pump inside tank, cross-section of pump.

The simulation set-up is outlined in Figure 9. The subject pump is simulated inside a volume of fluid to represent it being submerged. A short pipe of similar length to the test-rig is connected at the inlet. A long pipe section at the pump outlet is used to simulate the long pipe connection between it and the destination tank. A polyhedral mesh is used for the pump and connecting pipes. A surface trimmer mesh is used for the tank to improve continuity of the simulation but at a small increase of computational cost. Surface and volume controls to selectively refine different areas inside the pump. A systematic grid sensitivity study is carried out to reduce discretisation errors by following the standard set by the ASME Journal of Fluids. The basic definition for the terms in this grid convergence study could be found in the work authored by Celik (2005).

In the grid convergence study, the cells are refined at the impeller as this was found to have the greatest influence in agreement with the results. The monitored values used in this mesh study are the pump transient pressure outputs of at the beginning of the simulation, as it gives the best indicator of any fluctuations in the pressure results due to grid discretisation errors. The boundary conditions of the study are carried out at a rotation speed of 2900 RPM, flowrate of 0.28 l/s.

Mesh Parameter	Healthy	Moderate	Severe
Cell Count – Pump Mesh	2.23E+06		
Cell Count – Tank Mesh	1.31E+05		
Cell Count – Fine (N_1)	1.99E+07	2.12E+07	3.20E+07
Cell Count – Medium (N_2)	5.92E+06	5.99E+06	1.00E+07
Cell Count – Coarse (N_3)	1.70E+06	1.75E+06	3.12E+06
Ratio (Medium/Fine) r_{21}	1.50	1.52	1.47
Ratio (Coarse/Medium) r_{32}	1.51	1.51	1.48
Global p	1.89	5.22	4.24
p range	0.08 - 3.73	3.30 - 6.61	1.58 - 7.44
Max. GCI Error %	2.36%	1.24%	2.53%
Max. Error Value	0.41m	0.17m	0.30m
Avg. GCI Error %	0.80%	0.60%	0.90%
Avg. Error Value	0.14m	0.09 m	0.11m

Table 2. Parameters used in Grid Convergence Study.

Table 2 provides a summary of the parameters employed in the Grid Convergence Study. The terms healthy, moderate, and severe denote the level of impeller erosion. Whereas fine, medium, and coarse refer to the total cell counts from both the first and second stage impeller meshes.

The tank and pump mesh cell counts remain relatively constant for all erosion levels as there are no significant changes to their geometry. Since erosion changes the impeller's geometry, the cell counts for the three erosion cases are not the same. This is especially true for the severely eroded impeller, where the abundance of sharp edges significantly increases the cell count.

The refinement ratio r is calculated using the cell count of the impeller mesh for each erosion case. A refinement ratio of 1.5 is used to enable a sufficient level of differentiation between the three meshes used for each erosion level.

Figures 11, 12 and 13 outline the top view of a sample first-stage impeller and the suction side of a pump blade for three different levels of erosion: healthy, moderate and severe. On the left-hand side of each figure contains three images showing the impeller with coarse, medium and fine meshes. The graph on the right-hand side in each figure shows the results of the GCI study for each mesh.

For the healthy impeller with no erosion, the global order of accuracy for the numerical solution is p = 1.89, ranging from 0.08 to 3.73 for local order of accuracy p. Numerical uncertainty according to the Grid Convergence Index (GCI) is 0.80% on average, with a maximum discretization uncertainty of 2.36%, corresponding to a value of ±0.14m and ±0.41m of head at t = 0.045s respectively. The primary regions which exhibit the largest uncertainty are between t = 0.045s and t = 0.050s as highlighted by the error bars in Figure 11.

For the moderately eroded impeller, the global order of accuracy for the numerical solution is p = 5.22, ranging from 3.30 to 6.61 for local order of accuracy p. Numerical uncertainty according to the Grid Convergence Index (GCI) is 0.60% on average, with a maximum discretization uncertainty of 1.24%, corresponding to a value of ±0.09m and ±0.17m of head at t = 0.02s respectively. The primary regions which exhibit the largest uncertainty are between t = 0.010s, t = 0.020s, t = 0.030s and t = 0.055s as highlighted by the error bars in Figure 12.

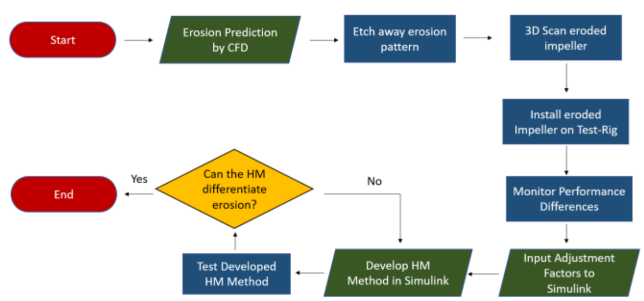

Figure 10. Flowchart outlining use of the HM test-environment.

For the severely eroded impeller, the global order of accuracy for the numerical solution is p = 4.24, ranging from 1.58 to 7.44 for local order of accuracy p. Numerical uncertainty according to the Grid Convergence Index (GCI) is 0.90% on average, with a maximum discretization uncertainty of 2.53%, corresponding to a value of ±0.11m and ±0.30m of head at t = 0.035s respectively. The points which exhibit the largest uncertainty are on t = 0.025s, t = 0.030s, t = 0.035s and t = 0.050s as highlighted by the error bars in Figure 13.

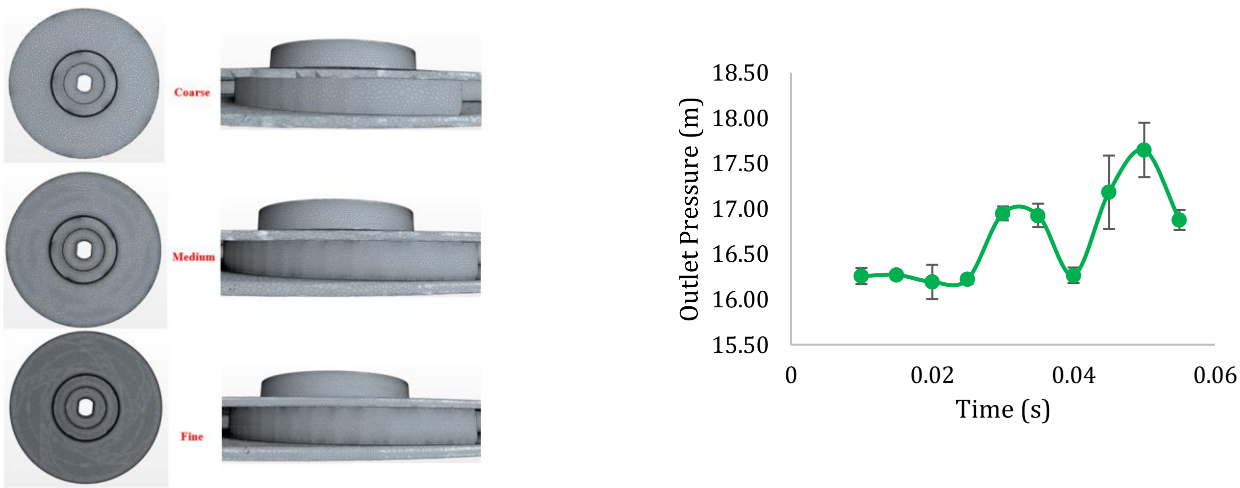

Figure 11. Healthy impeller meshes used for GCI study (left) and its results (right).

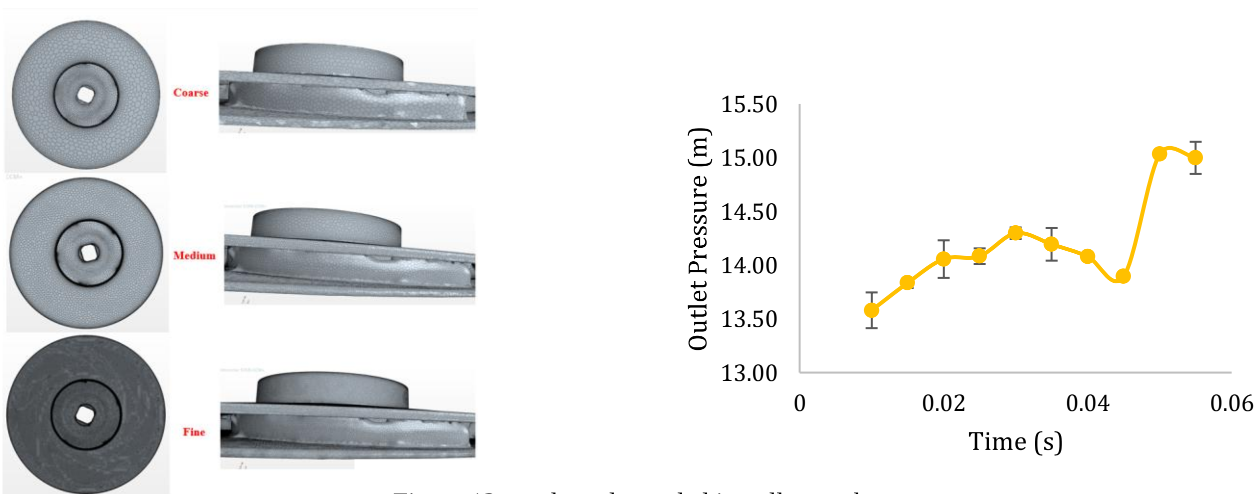

Figure 12. moderately eroded impeller meshes used for GCI study (left) and its results (right).

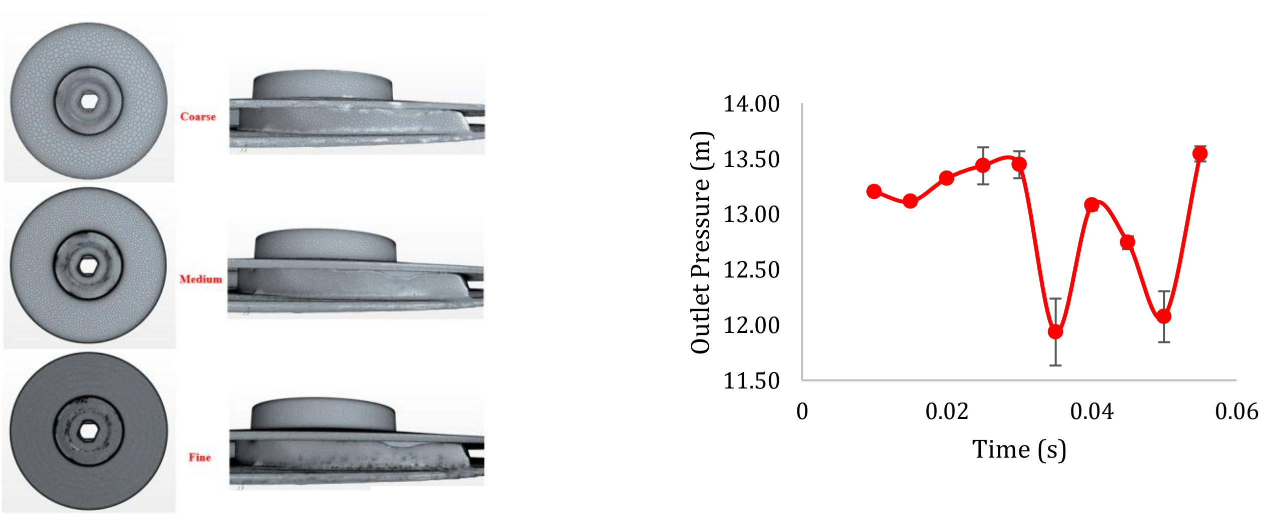

Figure 13. Severely eroded impeller meshes used for GCI study (left) and its results (right).

3.4. Experimental Procedure

The main purpose for the methods proposed is to develop a strategy to diagnose for cavitation erosion using a hybrid-based HM. The purpose of the tests carried out in the experimental rig is aimed to verify the accuracy of the CFD simulations and the system model running on Simscape.

Different types of sensors are placed across the test-rig so that the performance penalties and differences caused by cavitation erosion can be captured, and an HM mechanism can be developed to detect for this specific fault. The motor currents, pressure, flow and temperature across the pump are monitored. The test rig sensors have been selected based on a literature review on pump degradation mechanisms outlined in Section 2. The test pump is chosen as its design and performance envelope follows the specification of future airframe fuel pumps. The sensors are also chosen based on not only on their success for detecting similar faults, but also their suitability for installation on the aircraft fuel system environment. There is also a knowledge-gap related to erosion HM on two-stage pumps and the findings from this paper and future research will attempt to address this lack of knowledge.

In addition to experimental test rig data, results from a test-rig simulation and pump CFD model are coupled to the development of the HM detection mechanism. The CFD simulation is used to predict the areas inside the pump that are most susceptible to cavitation erosion and validate head and flow rate performance of the pump.

The performance degradations caused by the pump erosion provide the adjustment factor to the system model that is being run on Simscape. An example is with the pump outlet pressure loss observed at moderate impeller degradation. The same degree of pressure loss is represented in the Simscape model by modifying it with a suitable block to represent the change. The four sensors are initially chosen to conduct HM are temperature, flowmeter, pressure and current sensors. Temperature sensing is carried out with a thermal imaging camera on the BLDC motor coils. The flowmeter and pressure sensors are used as it is initially used to select the pump operating point. The current sensors are installed in each of the three motor phases as it allows ESA to be conducted for each of them. The primary disadvantage of ESA is that it has relatively lower signal-to-noise ratio (SNR) compared to the other methods, but these shortcomings can be remedied by using the appropriate signal condition and processing techniques (Benbouzid, et al., 2021).

Figure 10 summarizes the sequence of simulations and experiments carried out in this work using the test-rig, CFD and Simscape model. The sequence starts by running the erosion prediction in CFD. First, the boundary conditions are set to replicate the cavitation experimental work by Dular et al. (2006). These set of operating conditions are representative of in-service pumps experiencing cavitation.

The pump impeller blade surfaces are etched away around the leading and trailing edges of the impeller as predicted by the erosion model running on CFD. The 3D scan of the damaged blade is then re-meshed for subsequent CFD analysis so its performance differences can be studied. Once 3D scanning is complete, eroded impeller components are re-installed on the test-rig for the experimental campaign to generate data. Section 3.6 provides further detail on the operating conditions and impeller combinations used during testing. The pump CFD simulations and the test-rig experimental runs are conducted under equal boundary conditions so that differences between the results are directly comparable. This is repeated for healthy and eroded impellers. Additionally, the test rig will have multiple repeats runs after re-assembly to quantify to what degree the component installation influences sensors data results.

Once the checks between the CFD and test-rig results are satisfactory, the adjustments are implemented to the validated Simscape model in its healthy state. The changes to the model represent the damage caused by the eroded components and allow modal analysis to the HM parameters of interest: current, pressure and flow signals. The adjustments can be in the form of an additional block component or implementing some form of mathematical function in the existing model blocks that would reflect the performance degradation caused by the fault. A hybrid-based HM algorithm can then be developed to the relevant parameters that have been influenced by the erosion and differentiate between the three levels of component erosion.

Based on the current, flowrate and pressure data from the test-rig and combined with simulation model and CFD data, the effectiveness of the HM technique is evaluated. A key evaluation criterion is the ability to distinguish the different levels of erosion, under various pump operating conditions, with different sensors and model data inputs to the HM algorithm.

3.5. Fault Level Definition

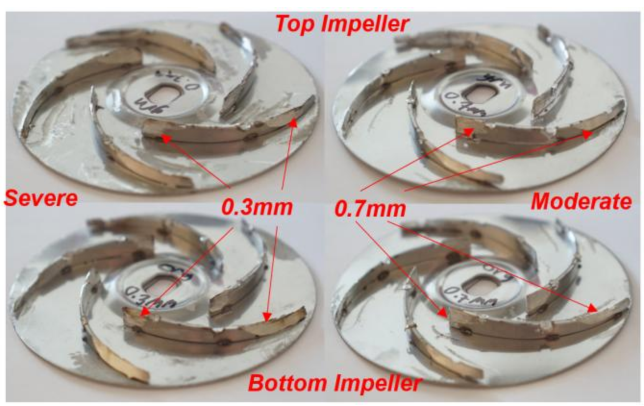

Figure 14. Impeller with damage at blade LE and TE.

The severity of pump erosion is defined by the of depth thickness remaining on the impeller measured in mm. Two levels of erosion severity are considered and have been based on the works of Wang et al. (2011). They are classed as 'Healthy', 'Moderate' and 'Severe', with the healthy case representing a new pump that has just entered service. The blade has an initial thickness of 1.5mm across the entire blade before any erosion damage is applied, which is defined as the 'Healthy' impeller. As highlighted by Figure 14, the 'Moderate' case has a 53% thickness eroded, with 0.7mm of material thickness both at the Leading Edge (LE) and Trailing Edge (TE) remaining. This represents a pump that has suffered cavitation and is at the middle of its useful life. The 'Severe' case has an 80% thickness eroded, with 0.3mm of material thickness remaining at the LE/TE. The latter represents a pump that has experienced significant cavitation erosion and is towards the end of its useful life. The photos in Figure 14 outlines the various stages of erosion damage compared with a healthy sample. The red arrows highlight areas which have been eroded away by cavitation and the numbers indicate remaining thickness because of the erosion.

3.6. Initial Baseline Tests

This section presents pump performance results from the test rig, simulation models and compares them. Additionally, electrical frequency spectral analysis results for healthy impeller conditions based on experimental tests and model simulations are presented.

Speed (RPM)	Flowrate (l/s)
2900 RPM	0.28, 0.56, 0.84, 1.12, 1.40, 1.68, 1.96
3500 RPM	0.56, 0.84, 1.12, 1.40, 1.68, 1.96, 2.24

Table 3. List of pump operating points.

Varied Parameter	Values	Research Question
Tank Head Level	0m, -0.2m, +0.2m	How does the different head level vary the pump performance?
Motor Speed	2900 RPM, 3500 RPM	How does the speed vary the pump performance?
Re-Assembly Count	2	How does the overall pump performance at each successive re-assembly?

Table 4. List of varied parameters.

For each cavitation erosion level, the pump is run at seven different pump operating points to their corresponding speed highlighted in Table 3. These points are selected based on the manufacturer's specified pump performance envelope. The flowrate intervals have a value of 1 m^3/h between each flowrate point. As outlined by the curves in Figure 15a, it was found that this interval provided sufficient resolution to define the pump head-flow curve. More data samples between the flowrate intervals specified in Table 3 are possible during the HM fault tests. This would only be done if the data from initial test regime suggests that conducting HM at these datapoint would generate signals with higher SNR and distinguishable modal frequencies. The goal is to collect baseline data under normal operating conditions before the erosion tests are carried out.

The seven points give the ability for comparison between whether erosion is easier to detect when the pump is operated at a higher flowrate but lower output pressure, or the opposite. The tests are run at different tank levels and motor speeds, as well as number of assemblies, to see how the pump performance envelope defined by Table 4 changes when these conditions are varied. Three tank levels are defined as +0.2 m, 0 m and -0.2 m to understand if static pressure at the inlet influences the accuracy and precision of the HM readings. At each of those head levels the same tests are repeated at 2900 RPM and 3500 RPM. To check variabilities from reassemblies, the sweep of tests is repeated, but after the pump is dismantled and rebuilt again with new seal components. The latter is to ensure that small changes in the pump assembly does not affect the experimental result. It was found that varying the static head did not have a significant influence on the result. When the same tests are repeated, and so static head was eliminated as a test variable.

4. RESULTS AND DISCUSSION

This section presents pump performance results from the test rig, simulation models and compares them from the three different erosion levels. Additionally, electrical frequency spectral analysis results for healthy impeller conditions based on experimental and model simulated conditions are presented.

4.1. Comparison of Test-Rig and Datasheet

Figure 15a outlines the pump head-flow curve comparing the results from the test-rig with the manufacturer's datasheet under two speeds. Very close agreement is achieved between the test-rig and datasheet, despite the slight differences in the setup and equipment used. The average error between the test-rig output and manufacturer specification is 3.5% and a maximum value of 7.1%, Disagreement between the datasheet and test-rig results are due to the test-rig being a pump in submerged in a tank, whereas the datasheet values are based on a closed loop pump system setup. The closed loop setup will induce a backpressure at the pump inlet, which is more prevalent at higher operating heads and results in a reduction in the head output.

Figure 15b compares the results between the calibrated test-rig simulation model and the test-rig experimental data. By using the test-rig data as input parameters to the pump block, leads to a very close agreement between the two methods. The pressure error measurements depicted by Figure 15b have an average and maximum values of 0.8% and 1.4% respectively.

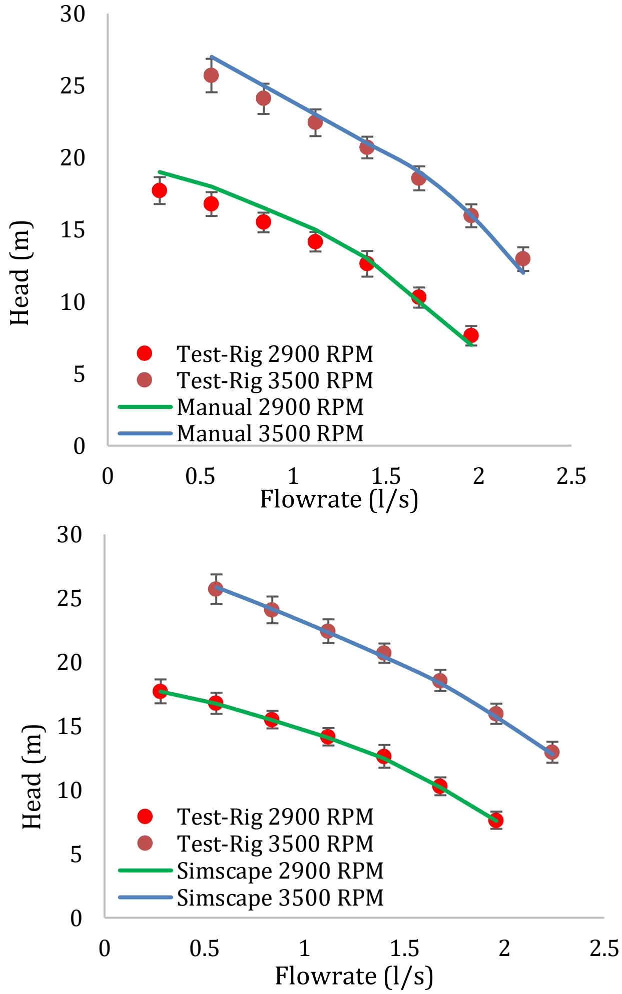

Figure 15. Pump performance results from test-rig and manual (top), test-rig compared with Simscape (bottom).

4.2. Comparison of Test-Rig, CFD and Simscape Model

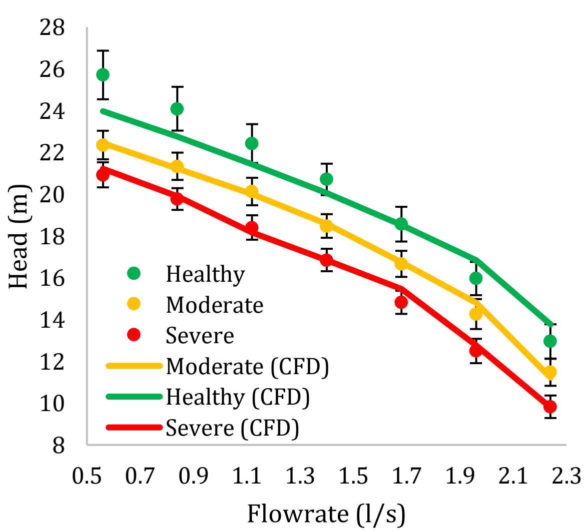

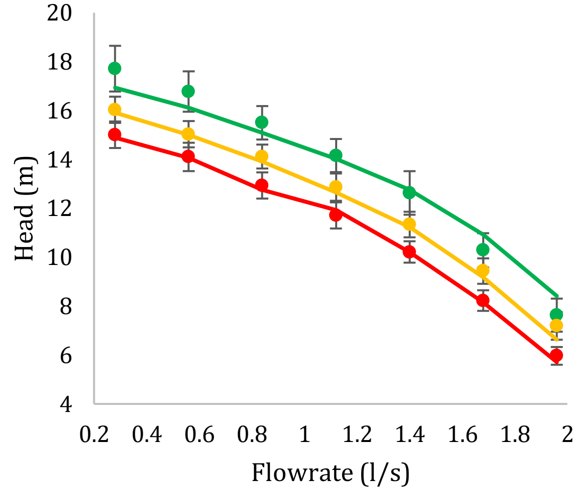

Figure 16. Pump head-flow curve comparing test-rig experimental with CFD results when motor is running at 3500 RPM (bottom-left) and 2900 RPM (top-right).

Figures 16a and 16b compares the pump flow curve that was generated via the CFD model with experimental data from the test-rig for the three erosion levels. Each coloured line represents one of the three different erosion levels; red for severe, yellow for moderate and green for healthy. The results from both methods show good agreement and still within the uncertainty of measurements of the test-rig pressure sensors, with an average uncertainty value of 0.85m of head. The uncertainty of the pressure sensors is due to the turbulent flows of the fluid that cause oscillations in the pressure measurements, which are greater than the quoted accuracy of the sensors of 0.2% of its maximum rated value. The discrepancies between the two results are caused by the complex fluid interactions of the inside the pump which are not fully captured in CFD. The flow and head ranges are selected as this is the intended operating range of the pump as specified in the datasheet.

For the datapoints, there is an average sensitivity of more than 6% between the different erosion severities from both test-rig and CFD data for both 3500 RPM and 2900 RPM cases. As this is higher than the minimum threshold sensitivity value of 5%, there is sufficient level of differentiation between the different erosion states that pressure could be used as reliable indicator for HM. This minimum sensitivity value for differentiating the levels of erosion on time-domain data is selected based on the previous works by Ezhilarasu, Skaf, & Jennions, (2021) and Niculita, Jennions, & Irving, (2013).

The data indicates that test-rig and CFD results are closely aligned, with an average error of 2.5% between the two methods. The largest discrepancies occurred at higher flow rates, with a maximum error of 10.28% for the 1.96 l/s, 2900 RPM case and 6.32% for the 2.24 l/s, 3500 RPM case. Additionally, under low flow conditions at 3500 RPM, CFD underestimated the pressure, resulting in a significant error of

6.74%. The greatest errors were observed for the healthy impeller in both RPM scenarios, while better agreement between CFD and test-rig data was achieved for the eroded impellers.

For the test-rig results outlined in all Figures 15 and 16 varying the head level from 0m, +0.2m and -0.2m static head does not make a significant difference to the pump performance, provided sufficient water level above the snorkel to prevent vortex formation and air entrainment. These values of static head are chosen as the tank height is 0.4 m and the pump is positioned 0.1 m above ground level. Having a change of 0.2 m in water level allows the static head to be varied, prevent overflow and be at the minimum water height above the pump inlet for smooth flow. Changing the static head and re-assembling the pump did not yield a significant difference in the results. The graphs outlined in Figure 16a and 16b is an average of those variations in static head and after re-assembly, as outlined in Table 4. The pressure error measurements depicted in Figure 16a and 16b between the CFD and test-rig results have an average and maximum values of 2.5% and 10.3%, respectively.

4.3. Current Signature Readings

Figure 17a compares the flowrate with the RMS current of a single phase. As highlighted, there is high degree of alignment when observing the RMS current with its corresponding flowrate value. The average current measurement uncertainty value is 0.49A for the 2900 RPM case and a value of 0.57A for the 3500 RPM case taking into the errors from the current ripple and standard deviation. The average error between the Simscape and test-rig results is 0.80% and the maximum error is 0.94% across all flowrates. The error for flowrate and pressure measurement is 0.05%. The uncertainty is comparatively lower for the 2900 RPM relative to the 3500 RPM case due to the lower variation from the sampled current values.

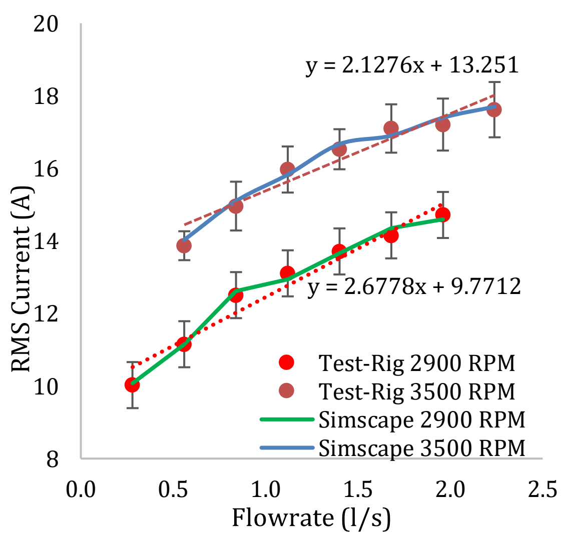

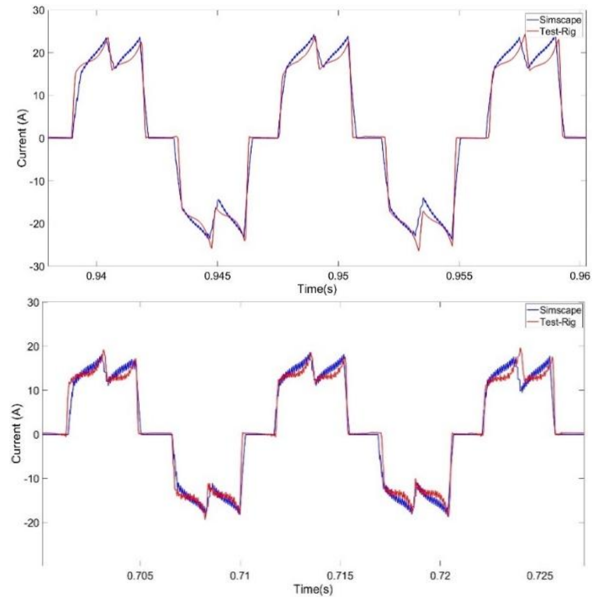

Figure 17. Motor current signatures from test-rig vs. Simscape. Graph for RMS current (bottom-left), 3500 and 2900 waveforms (top-right)

Figure 17b and 17c depicts the pump motor signature from a single current phase for 3500 RPM case (top) and 2900 RPM case (bottom). The current signatures from the experimental data are well-aligned with the results from the Simscape simulation. The speed of the motor can be inferred using the frequency of each current phase and number of poles of the BLDC motor. The pump flowrate can also be inferred from the current waveform RMS values, the higher the flowrate, the larger are the current values. This is due to higher flow resistance at higher flowrates which incites the motor to generate higher torque values to overcome it and regulate the same speed setpoint. Since torque and phase currents are directly proportional in a BLDC motor, the increase in torque leads to an increased current (Rajagopalan, Aller, Restrepo, Habetler, & Harley, 2006). The current graphs depicted in Figures 17 and 18 are when the pump is running at a flowrate of 1.96 l/s for both 3500 RPM and 2900 RPM cases.

The motor phase current envelope output in Simscape is influenced by several parameters: controller architecture, pump operating points, PWM switching frequency, as well as motor resistance and inductances. The differences in spurious fluctuations from the current values are due to the PWM switching operating at approximately 50% of its maximum duty cycle at 2900 RPM, and near 100% at 3500 RPM. The pump flow operating point determines the overall current draw from the motor. Observing the current ripples on Figure 17 would imply that conducting ESA at higher RPM speeds would in theory be more reliable as the current measurements has lower noise from the reduced current ripple. This however does not happen, due to the increased variation in sampled current at higher rotation speeds. Since current and flow are linearly tied, the higher flow turbulence observed in the 3500 RPM case lowers the precision from the current samples, resulting in a higher standard deviation. The increased error caused by this offset the lower errors from the current ripples and yields a higher overall error on all datapoints for the 3500 RPM case.

The simscape model can represent the changes in current that result from changes in the flow. This means that any current irregularities because of the erosion faults, can be captured by the model, and an HM scheme can be developed around it. Providing input data to an HM capability through a simulation model allows the fault and detection schemes to be tested under much wider boundary conditions, including those not possible on the test-rig setup.

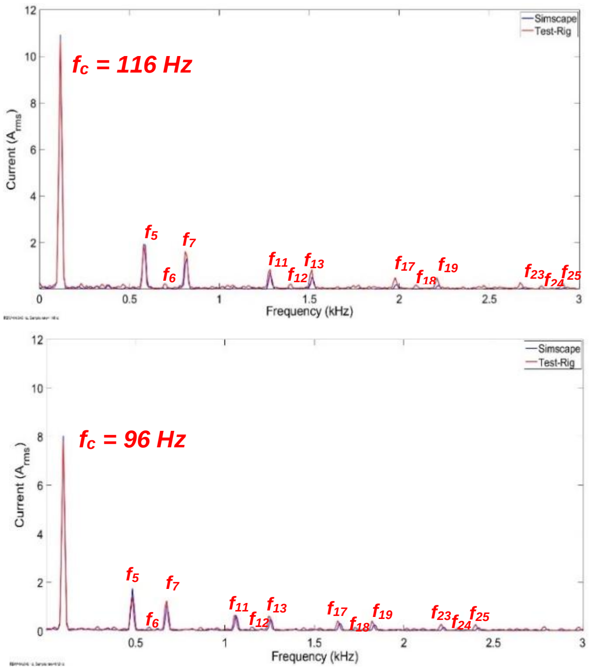

Figure 18. Electrical frequency spectra from Test-Rig vs. Simscape.

Figure 18 outlines the frequency spectra from the same signals outlined in Figure 17 by carrying out Fast Fourier Transform (FFT) for 3500 RPM case (top) and 2900 RPM case (bottom). This process dissects the time-domain signal into its sinusoidal components and highlights the intensity for each of those constituent signals. This method allows identification of any additional modal signals induced by a fault, as the fault will generate a signal unique at some frequency outside of the baseline spectral pattern. The FFT is carried out using Chebyshev filter due to its low noise at higher frequencies relative to f_c (Gaydecki, 2004). The range is selected to 3 kHz as according to observation, the signals beyond this frequency would have been significantly attenuated for meaningful analysis. As highlighted by the frequency signature, the signals appear at conjugate patterns and at discrete multiples of the fundamental frequency, f_c. This critical frequency corresponds to the rotational speed of the motor divided by the number of pole pairs, which in this situation is 2. 2900 RPM corresponds to a rotational speed of 48 Hz, and 3500 RPM to 58 Hz. Multiplying with 2 pole pairs yields a value of 96 Hz and 116 Hz, which is the value of f_c for their respective RPM cases for the frequency spectra graph.

Figure 18 also highlights that the signals appear in conjugate pairs. The model does not show an amplitude at this frequency, whereas the test-rig results express a very small magnitude. The significant amplitudes occur at the odd conjugate frequencies which are located at +1$\boldsymbol{f_c}$ and -1$\boldsymbol{f_c}$, that centres the 6th multiple of $\boldsymbol{f_c}$ such as the 6th, 12th, 18th and 24th harmonic. For each of those respective harmonics, the conjugate pairs appear on the 5th & 7^{th,} 11th & 13th,17th & 19th and 23rd & 25th harmonic. Since the time-domain signal is trapezoidal, and bears close relation with a square wave, it will have similar constituent signals. The frequency signatures are consistent with square wave theory as it is expressed as the sum of sinusoidal waves at odd frequency integers with attenuating amplitudes, as the harmonic number increases (Gaydecki, 2004).

There are some differences between the simulation model and experimental results even after successful calibration. For the frequency-domain results, there is better agreement than the time domain results, where the values of the signal frequency and amplitude from the model closely follow the test-rig results. The primary difference between the results are the values of the amplitude of the even harmonic components at the 6th, 12th, 18th and 24th harmonic components. The primary difference from this is likely due to the sharp gradation of the slope in the time-domain, which may have increased the amplitude of the signal, even if it is a small value. Another difference is the very slight phase shift between the model and test-rig results, which are more apparent at higher frequency. This is due to the torque ripple caused in the test-rig and the spurious flow which may cause a slightly deviation in the motor speed from its setpoint speed of 3500 RPM.

For the time-domain results, a difference between the model and test-data is in the approximation of the current rise from each phase. The shoulder of the waveform peak refers to the 12A point for the 2900 RPM case and 15A point for the 3500 RPM case. Inspecting the peak current values in Figure 17, The estimation of current rise (di/dt) from the shoulder of the peak to very tip of the current waveform has a slight discrepancy between the model and test-rig results. In the test rig there is a convex curvature as the current reaches peak values, whereas for the Simscape model, the curvature is closer to a linear slope. The magnitude of difference is in the order of approximately 2A in this transient region for the time-domain waveform. Inspecting the FFT results in Figure 18, the mentioned difference in the current profile only yields small amplitude increase in the even harmonic components, but both waveforms still have the same frequency components and are largely in-phase. This further emphasizes that the slight differences in the waveform envelope will not have a significant impact to the quality of analysis when carrying out HM in the Simscape model.

The mentioned differences in the time-domain waveform are caused by the way the model approximates the motor circuit. The simulation model approximates the BLDC circuit as a Resistance-Inductor (RL) circuit to represent the magnetic components. This approximation, although generally accurate to model the dynamics of the motor, does not include the magnetic saturation behaviour as the motor reaches its set-point speed (Atay, 2000; Korkosz, Bogusz, & Prokop, 2018; Jang, Choo, & Choi, 2007). This explains the convex curvature of the current ripple found on the test-rig data. Regardless of this difference, the Simscape model has reached a sufficient level of fidelity, as the comparative differences in the current profile as a result of the erosion damage can still be captured. This is further emphasized in the results outlined in Figure 16b, where the RMS output of the current changes depending on the pump flowrate, highlighting how changes in fluid flow can be translated to electrical domain.

4.4. Temperature Sensor Readings

Figure 19 summarises the temperature readings across different flowrates for the two motor rotation speeds. Each coloured line represents one of the three different erosion levels; red for severe, yellow for moderate and green for healthy. The top graph represents the 3500 RPM case and bottom represents the 2900 RPM case. As outlined by the results, there is significant temperature fluctuation even when no fault is introduced. There is also no consistent pattern related to the system flowrate and the temperature measured at the BLDC motor. Most of the temperature fluctuations observed are due to changes to the ambient temperature, which directly affects the reading from the temperature sensor. As a result of this finding, temperature is not a monitored parameter for HM and its behaviours are also not included in the simulation models used.

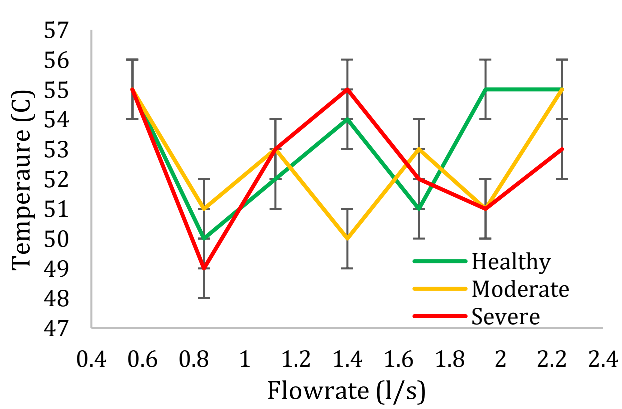

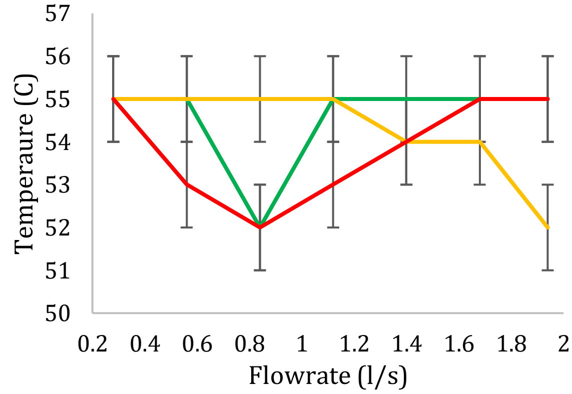

Figure 19. BLDC Motor temperature for two speeds, 3500 RPM (bottom-left) and 2900 RPM (top-right).

4.5. Summary of Results

The presented results characterize the pump under healthy operating conditions, to establish baseline HM indicators under normal operation. The disagreements between the motor model in Simscape and the unit installed in the test-rig, is due to their full specifications to not being disclosed by the manufacturer, resulting in minor differences. The pump flow characteristics from the test-rig and CFD results showed better agreement than the results between the test-rig and manufacturer datasheet. The flow data outlined in the manual had differences in its test installation, which have contributed to the disagreement between the two results. The pump in the test-rig was submerged, whereas the pump in the test datasheet was not submerged and was directly connected to a pipe. The experiment and simulation result showed best agreement at median flowrates, which are the operating points between 1.12 l/s to 1.68 l/s.

A good level of sensitivity has been demonstrated based on the pressure readings, as the differences for each flow data point was approximately 6%, higher than the minimum 5%. The CFD simulation results also show close agreement with the pressure measurements, meaning that it can be used to reliably model pump impeller degradation.

At high flowrates (>1.68 l/s) the minor discrepancy between the experimental and simulation data is due to the average interpolation method used by CFD to calculate pressure and velocity transitions in the boundary interface. As a result, some small-scale vortices and energy transfer that occur in the test-rig may have been ignored in the CFD predictions.

At low flowrates (<0.84 l/s), the head prediction shows the highest discrepancy, with a disagreement of 10.3% for 2900 RPM case and 6.7% for the 3500 RPM case. This is because based on the moody diagram (Moody, 1944), the flow is not completely turbulent, with portions of the flow being laminar, i.e., in the transition region. This is indicated by the Reynolds number of $Re < 3.0 \times 10^4$ and relative roughness, (ϵ/d) of

0.0005 from the PVC pipe is indicated on the moody diagram. The CFD code on the other hand, utilises RANS modelling which assumes that the flow is fully turbulent and cannot predict laminar flows. The boundary layer growth rate caused by laminar flows are different to that of turbulent flows, resulting in different gradients on the surface. This leads to different wall shear stresses and separation that alter the flow (Schlichting & Gersten, 2017). As a result of these differences, CFD cannot predict the flow as accurately in these lower flowrates.

It was found that changing the static head and successive re-assemblies of the pump had minor variations to all the parameters being monitored for HM. All the graphs on Figures 15 and 16 represent the average from both re-assemblies and different static head levels being tested. Any differences are more likely to be attributed to the random errors as a result of the turbulent flows across the test-rig. The very minor deviations caused by re-assembly is proven true when pump gasket and annular seals are replaced.

The accuracy advantages of carrying out HM closer to maximum rotation speed is negated because the higher flow turbulence that reduces the precision of the readings. Since current and flow are tied, the flow oscillations create variations in the current readings. These disturbances create random errors that offset the accuracy gains from the reduced current ripple as highlighted by the 3500 RPM case.

As highlighted in section 4.4, the temperature results show high variability in the results across the different erosion levels. In addition to this, the data from the different erosion levels overlap and show no sensitivity to the fault. As a result, temperature is not used for HM, and its behaviour is not included in the models used.

5. CONCLUSION

This paper has described a hybrid-based HM test environment setup, to simulate cavitation erosion with a combination of experimental test-rig, pump CFD and simulation models. It has also demonstrated the novel use of how a BLDC motor can be used to detect changes in flowrate and how it could be used to capture the performance penalties resulting from erosion. A high-level of agreement has been achieved between CFD simulations and test-rig results. It was found that the test-rig results show less agreement with the CFD simulation than the flow curve suggested by the manual provided by the manufacturer. The discrepancies between the CFD and test-rig results are due to inherent limitations of CFD in resolving the complex flow interactions in the pump. The discrepancies between the test-rig results and manufacturer data are due to the slightly different test setup used. Other relationships have also been discovered:

•The use of a BLDC motor allows the pump flowrate and RMS current to have a generally linear relationship.

•The dynamics at peak current values differ slightly between simulation and experiment, but RMS values between the two are well-aligned.

•Carrying out ESA at closer to its maximum speed is less reliable as the random errors caused by the increased flow turbulence increases precision errors.

•Pump outlet pressure measurements can be used to detect pump impeller erosion with a good level of sensitivity.

•CFD can be used to accurately model the pressure degradation of a pump after it experiences impeller erosion.

•CFD under-estimates pressure slightly at lower flowrates and overestimates it at higher flowrates relative to rig measurements.

•Pump motor temperature readings show no sensitivity towards detecting impeller erosion.

With the discovered relationships between motor current and flowrate, it is expected that the degradation in flow and pressure as a result of erosion can be captured in ESA. This relationship is more easily observable with a BLDC motor, as its current output is highly sensitive to changes in the load. In addition to the flow and pressure changes caused by erosion, there will be transient signals generated resulting from the erosion from both the electrical and fluid-mechanical domain.

5.1. Future Work

The continuation of this work involves carrying out experiments using the eroded impeller on both the CFD and test-rig setups, specifically to monitor pressure and amplitude fluctuations over its steady state values. The changes as a result from the mentioned tests will then inform what kind of parameters to adjust to represent the same abnormality in Simscape. Re-creating the fault on the latter software allows model-based health monitoring, which allows more sophisticated HM schemes and strategies to be developed as well as experimentation with boundary conditions not physically possible on the test-rig. The validated CFD model under faulty conditions can fulfil a similar role to the Simscape model, but the latter is able to do the model-based HM in the fluid-mechanical domain with higher fidelity. The Simscape model is particularly advantageous due to the BLDC model as well as other components in other domains such as fluid mechanics.

ACKNOWLEDGEMENT

This research is funded by United Kingdom Research and Innovation (UKRI), grant no. EP/L016389/1. *All data underlying the results are available as part of the article and no additional source data are required.*

NOMENCLATURE

σ	Cavitation number
ρ	Density
α	Vapor Fraction
P	Pressure
Q	Flowrate
P_v	Saturation Pressure
v	Velocity
t	Time
f_c	Fundamental Frequency
BLDC	Brushless DC Motor
CFD	Computational Fluid Dynamics
CT	Current Transformer
ESA	Electrical Signature Analysis
FFT	Fast Fourier Transform
GLM	Gray Level Method
HI	Health Indicator
HM	Health Monitoring
LE/TE	Leading/Trailing Edge
RMS	Root Mean Square
SNR	Signal-to-Noise Ratio
Star-CCM+	CFD Software Package
UAV	Unmanned Aerial Vehicle
EMF	Electromagnetic Force.

REFERENCES

Adamkowski, A., Henke, A., & Lewandowski, M. (2016). Resonance of torsional vibrations of centrifugal pump shafts due to cavitation erosion on impeller. *Engineering Failure Analyses, 70*, 56-72.

Addie, G., & Sellgren, A. (1998). The Effect of Wear on the Performance of Centrifugal Slurry Pumps. *Proceedings of ASME Fluids Engineering Division Summer Meeting.* Washington.

Atay, F. (2000). Magnetic Saturation and Steady-State Analysis of Electrical Motor. *Applied Mathematical Modelling, 24,* 827-842.

Bachert, B., Ludwig, G., Stoffel, B., Sirok, B., & Novak, M. (2003). Experimental Investigations Concerning Erosive Aggressiveness Of Cavitation In A Radial Test Pump With The Aid Of Adhesive Copper Films. *Fifth International Symposium on Cavitation.* Osaka.

Benbouzid, M., Berghout, T., Sarma, N., Djurovic, S., Wu, Y., & Ma, X. (2021). Intelligent Condition Monitoring of Wind Power Systems: State of the Art Review. *MDPI: Energies, 14*(5967).

Bross, S., & Addie, G. (2002). Prediction of Impeller Nose Wear Behaviour in Centrifugal Slurry Pumps. *Experimental Thermal and Fluid Science, 26,* 841-849.

Celik, I. B. (2005). *Journal of Fluids Engineering Editorial Policy Statement on the Control of Numerical Accuracy.* Morgantown: West Virginia University.

Chowdhury, S., Ali, F., & Jennions, I. (2023). Development of a Novel Ground Test Facility for Aircraft Environmental Control System. *ASME Journal of Thermal Science and Engineering Applications, 15*.

D'Agostino, L. (2011). *Turbomachinery Developments in Cavitation.* Pisa: Nato.

Dessena, G., Ignatyev, D., Whidborne, J., Pontillo, A., & Fragonara, L. (2022). Ground Vibration Testing of a Flexible Wing: A Benchmark and Case Study. *MDPI - Aerospace, 9*(8).

Deyou, L., Hongjie, W., Gaoming, X., Ruzhi, G., Xianzhu, W., & Zhansheng, L. (2015). Unsteady simulation and analysis for hump characteristics of a pump turbine model. *Renewable Energy, 77*, 32-42.

Dular, M., & Coutier-Degosha, O. (2009). Numerical Modelling of Cavitation Erosion. *International Journal for Numerical Methods in Fluids, 61*, 1388-1410.

Dular, M., Bachert, B., Stoffel, B., & Sirok, B. (2004). Relationship between Cavitation Structures and Cavitation Damage. *Wear, 257*, 1176-1184.

Dular, M., Stoffel, B., & Sirok, B. (2006). Development of a Cavitation Erosion Model. *Wear, 261*, 642–655.

Dular, M., Stoffel, B., & Sirok, B. (2006). Development of a Cavitation Erosion Model. *Journal of Wear, 261*, 642–655.

Ezhilarasu, C. M., Skaf, Z., & Jennions, I. (2021). A Generalised Methodology for the Diagnosis of Aircraft Systems. *IEEE Reliability Society Section*, 11437-11454.

Fortes-Patella, R., Reboud, J. L., & Briancon-Marjollet, L. (2004). Aphenomenological And Numerical Model For Scaling The Flowagrssiveness In Cavitation Erosion. *Workshop on Cavitation Erosion.* Val de Reuil.

Gaydecki, P. (2004). *Foundations of Digital Signal Processing: Theory, Algorithms and Hardware Design.* London: IET.

Ge, M., Svennberg, U., & Bensow, R. E. (2021). Improved Prediction of Sheet Cavitation Inception Using Bridged Transition Sensitive Turbulence Model and Cavitation Model. *Marine Science and Engineering*.

Hanusz, Z., & Tarasinska, J. (2011). Tables for Shapiro-Wilk W Statistic According to Royston Approximation. *Colloquium Biometricum, 41*, 211-219.

Hayward, A. (1979). *Flowmeters.* London: The MacMillan Press Ltd.

Hughes, A., & Drury, B. (2019). *Electric Motors and Drives: Fundamentals, Types and Applications.* Oxford: Elsevier.

International Organisation for Standardisation. (2012). *ISO 9906:2012 Rotodynamic pumps — Hydraulic performance acceptance tests — Grades 1, 2 and 3.* Geneva: ISO.

Jang, S.-M., Choo, H.-W., & Choi, S.-K. (2007). Design and Analysis of a High-Speed Brushless DC Motor for

Centrifugal Compressor. *IEEE Transactions on Magnetics, 46*(6), 2573-2575.

Jiao, X., Huang, B., Li, J., & Xu, G. (2017). Research on Fault Diagnosis of Airborne Fuel Pump Based on EMD and Probablistic Neural Network. *Microelectronics Reliability*(75), 296-308.

Kahlert, A. (2017). Specification and Evaluation of Prediction Concepts in Aircraft Maintenance. *University and State Library Darmstadt*, (pp. 1-37). Darmstadt.

Kehtarnavaz, N. (2008). *Digital Signal Processing System Design.* Amsterdam: Elsevier.

Korkosz, M., Bogusz, P., & Prokop, J. (2018). Modelling and Experimental Research of Fault-Tolerant Dual-Channel Brushless DC Motor. *IET Electric Power Applications, 12*(6), 787-796.

Li, T., & Van Terswiga, T. (2012). On the capability of a RANS Method to Asses Cavitation Erosion on a Hydrofoil. *Proc. of 8th International Symposium on Cavitation.* Singapore.

Mao, J. Y., Yuan, S. Q., Pei, J., Zhang, J. F., & Wang, W. J. (2014). Applications of different turbulence models in Applications of different turbulence models in with the diffuser. *27th IAHR Symposium on Hydraulic Machinery and Systems.* Montreal.

Maulana, F., Starr, A., & Ompusunggu, A. (2023). Explainable Data-Driven Method Combined with Bayesian Filtering for Remaining Useful Lifetime Prediction of Aircraft Engines Using NASA CMAPSS Datasets. *MDPI - Machines, 11*(2).

Messina, J., Cooper, P., & Heald, C. (2008). *Pump Handbook.* McGraw-Hill Publishing.

Mishra, P., Pandey, C., Singh, U., Gupta, A., Sahu, C., & Keshri, A. (2019). Descriptive Statistics and Normality Tests for Statistical Data. *Annals of Cardiac Anaesthesia, 22*(1), 67-72.

Moody, L. F. (1944). Friction Factors for Pipe Flow. *Transactions of the ASME, 66*, 671-684.

Niculita, O., Jennions, I., & Irving, P. (2013). Design for Diagnostics and Prognostics: A Physical-Functional Approach. *IEEE Aerospace Conference.* Big Sky.

Palgrave, R. (2019). VIsual Studies of Cavitation in Pumping Machinery. *Texas A&M University Library.* Texas.

Rajagopalan, S., Aller, S., Restrepo, J., Habetler, T., & Harley, R. (2006). Detection of Rotor Faults in Brushless DC Motors Operating Under Nonstationary Conditions. *IEEE Transactions on Industry Applications.*

Rayan, M., & Shawky, M. (1989). Evaluation of Wear in a Centrifugal Slurry Pump. *Proceedings of the Institution of Mechanical Engineers. Part A, Journal of Power and Energy.*

Sarma, N., Tuohy, P., & Djurovic, S. (2019). Modeling, Analysis, and Validation of Controller Signal Interharmonic Effects in DFIG Drives. *IEEE Transaction, 11*(2), 713-725.

Sarma, N., Tuohy, P., & Djurovic, S. (2021). Stator Electrical Fault Detection in DFIGs Using Wide-Band Analysis of the Embedded Signals From the Controllers. *IEEE Transactions On Energy Conversion, 36*(2), 800-811.

Sarma, N., Tuohy, P., Mohammed, A., & Djurovic, S. (2021). Rotor Electrical Fault Detection in DFIGs Using Wide-Band Controller Signals. *IEEE Transactions On Sustainable Energy, 12*(1), 623-633.

Schlichting, H., & Gersten, K. (2017). *Boundary-Layer Theory.* Berlin: Springer.

Sedlar, M., Zima, P., Bajorek, M., & Kratky, T. (2012). CFD Analysis of Unsteady Cavitation Phenomena in Multistage Pump with Inducer. *IOP Conference Series: Earch and Environmental Science, 2012.*

Shapiro, S., & Wilk, M. (1965). An Analysis of Variance Test for Normality (Complete Samples). *Biometrika, 52*(4), 591-611.

Skaf, Z. (2015). Prognostics: Design, Implementation and Challenges. *Twelfth International Conference on Condition Monitoring*, 340.

Sreedhar, B., Albert, S., & Pandit, A. (2017). Cavitation Damage: Theory and Measurements. *Wear*, 177-196.

Taylor, J. (1998). *An Introduction to Error Analysis.* Sausalita: University Science Books.

Usta, O., Aktas, B., Maasch, M., Osman, T., Atlar, M., & Korekut, E. (2017). A study on the numerical prediction of cavitation erosion for propellers. *Symposium of Marine Propulsion (SMP'17).* Finland: Strathclyde University.

Verhulst, T. (2023). *Health Monitoring Techniques to Diagnose for Cavitation Erosion.* Cranfield: Cranfield University.

Verhulst, T., Judt, D., Lawson, M., Chung, Y. M., Al-Tayawe, O., & Ward, G. (2022). Review For State-Of-The-Art Health Monitoring Technologies On Airframe Fuel Pumps. *International Journal of Prognostics and Health Management, 13*(1).

Verhulst, T., Ng, E., Chung, Y., Judt, D., & Lawson, C. (2022). Predicting Cavitation Erosion on Two-Stage Pumps Using CFD (GT2022-84165). *ASME Turbo Expo 2022: Turbomachinery Technical Conference and Exposition.* Rotterdam.

Visser, F. C., Dijers, R. J., & op de Woerd, J. H. (2000). Numerical Flow-Field Analysis and Design Optimisation of a High-Energy First-Stage Centrifugal Pump Impeller. *Computing and Visualisation in Science, 3*, 103-108.

Walker, C. I. (2001). Slurry Pump Side-Liner Wear: Comparison of Some Laboratory and Field Results. *Wear, 250*, 81-87.

Walker, C. I., & Roudnev, A. (2002). Slurry Pump Impeller Wear: Comparison of Some Laboratory and Field Results. *Proceedings of the 15th International*

Conference of Hydrotransport, (pp. 725-736). Banff.

Wang, Y., Zuo, M., & Fan, X. (2011). Design of An Experimental System for Wear of Slurry Pumps. *Proceedings of Canadian Engineering Education Association.* Kaninaskis.

Xu, H., Chen, W., & Xu, C. (2019). Cavitation Performance of Multistage Slurry Pump in Deep-Sea Mining. *AIP Advances: Fluid and Plasmas Collection, 9*, 1-17.

Yilmaz, N., Atlar, M., & Khorasanchi, M. (2019). An improved Mesh Adaption and Refinement approach to Cavitation Simulation (MARCS) of propellers. *Ocean Engineering, 171*, 139-150.

Ylonen, M. (2016). *Cavitation Erosion Characterization of Francis Turbine Runner Blade Material.* Tampere: Tampere University of Technology.

Yu, H., & The, J. (2016). Validation and optimization of SST k-u turbulence model for pollutant dispersion within a building array. *Atmospheric Environment, 145*, 225-238.

Zhang, D. (2017). Comparison of Various Turbulence Models for Unsteady Flow around a Finite Circular Cylinder at Re=20000. *The 2017 International Conference on Cloud Technology and Communication Engineering.* Guilin.

Zhu, J., & Zhang, H. (2017). *Numerical Study on Electrical Submersible Pump Two-Phase Performance and Bubble Size Modelling.* Tulsa: University of Tulsa.

BIOGRAPHIES

Tedja Verhulst recently graduated with an EngD and MSc degrees from Cranfield University. He also has an MEng (Hons) in Electronics engineering from the University of Manchester. Prior to his EngD, he worked in British Steel and Airbus. In British Steel he worked in the maintenance department, where he had to manage various assets in the steelworks, such as pumps and motors. In Airbus, he worked in the Fuel Systems department where he filed a US/UK patent at the end of his year there in health monitoring of fuel pumps. He also has worked in MBDA Systems in the actuators center of excellence.

David Judt is a Senior Lecturer in Airframe Systems Design in the Centre for Aeronautics at Cranfield University. He received a MEng in Aeronautical Engineering from the University of Glasgow in 2010, and joined Cranfield University in 2011 to complete his PhD in 2014. He now teaches aircraft systems and system design for assembly and manufacturing. He has contributed to large research projects, as Co-Investigator and researcher in fields of thermal-fluid models for evaluation of novel airframe systems, on a component and architectural level.

Craig Lawson is a Reader in Airframe Systems at Cranfield University, UK, and his teaching responsibilities include lecturing aspects of aircraft design and performance at postgraduate level. He has a BEng (Hons.) in Electrical and Mechanical Engineering from the University of Edinburgh, UK and a PhD in Aerospace Engineering from Cranfield University, UK. He has been Principal Investigator on 12 grants, with a focus on aircraft level impact of novel systems. He has published 70+ research papers. He is a CEng, FHEA, FRAeS.

Osama Al-Tayawe is fuel Systems engineer from airbus UK. He specialises in the fluid-mechanic side of fuel systems and has over 20 years' experience in the department. He has worked on various components in the fuel systems but specialises in fuel pumps and motor-actuated valves. He obtained his doctorate from Bristol University and has worked as lecturer King Fahd University of Petroleum and Minerals in Saudi Arabia. He has worked for almost aircraft programmes for Airbus from the A300, to the latest A350.

Geoff Ward is a fuel Systems engineer from Airbus UK. He specialises in the control and electronics of aircraft fuel pumps and has experience working on other avionics components within fuel systems. He joined Airbus in 2008 but has also worked for the company even longer as a consultant for the A380 program. Prior to working for Airbus, he worked as electronics engineer for various aerospace-related projects.

Yongmann M. Chung is an Associate Professor of Computational Fluid Dynamics (CFD) at the University of Warwick. His expertise is High Performance Computing (HPC) and CFD of turbulent flows. He has an MS, BS, PhD in Mechanical Engineering from KAIST, Korea. Dr Chung worked on several EPSRC projects on aircraft skin-friction flow control. His research team also developed medical-image based, patient-specific CFD modelling methodologies. Dr Chung has published over 100 journal and conference papers.